A comparison of modulation techniques and motor performance evaluation

Master's thesis in Electric Power Engineering

YANGDI HE

A comparison of modulation techniques and motor performance evaluation

YANGDI HE

Cover: Inverter power losses map of SVM using interpolation.

A comparison of modulation techniques and motor performance evaluation
YANGDI HE
Department of Electrical Engineering
Chalmers University of Technology

Abstract

In this thesis, several modulation techniques are implemented in a permanent magnet synchronous machine (PMSM) field-oriented control (FOC) drive system. Among them, third-harmonic injection PWM (THIPWM), space vector modulation (SVM) and discontinuous PWM (DPWM) show distinct behaviors in the system. Key parameters of the machine as well as the inverter are compared and evaluated. Current harmonics, inverter losses, inverter efficiency and switching frequency are included in the evaluation.

Primarily, phase current total harmonic distortion (THD) is analyzed using either manual FFT or the Powergui toolbox. The result shows that 1/6 THIPWM has more harmonics components than 1/4 THIPWM in most of the speed-torque area. Continuous PWM (CPWM) is proved to have higher linearity than DPWM in general under the same switching frequency. For DPWM, the THD decreases in the following order: DPWM0, DPWM1, DPWMMAX/DPWMMIN, DPWM3, DPWM2. For CPWM, the order is: 1/6 THIPWM, SVM, 1/4 THIPWM. However, DPWM2 can achieve even lower THD performance than CPWM in the high-speed region. In the low speed region, CPWM is still favorable.

Next, for inverter conduction losses, each method does not differ much. While for switching losses, DPWM has an advantage over CPWM and each DPWM method has a different characteristic in relationship with the phase angle. When the load phase angle is around zero, i.e., in the high power factor region, DPWM1 has the lowest switching loss. When the phase angle is relatively large and positive, i.e., mostly in the non-field-weakening region in the speed-torque map, DPWM2 shows the lowest switching loss. When the phase angle is relatively large but negative, i.e., mostly in the field-weakening region, DPWM0 has the best switching loss performance. Low switching losses lead to high inverter efficiency.

Furthermore, the ECE and EUDC driving cycles are applied to test the inverter performance in a real-life scenario. Neural network curve fitting and interpolation are both involved in the investigation. Total energy losses are compared between SVM and DPWM for the two driving cycles. Moreover, a comparison based on switching frequency variation is made to show how switching frequency affects inverter losses and the current THD. For DPWM, it is a trade-off between the switching losses and the current THD when it comes to the switching frequency.

Keywords: Modulation technique, SVM, DPWM, PMSM, MTPA, THD, inverter, losses, efficiency, driving cycle.

Acknowledgements

This thesis is conducted at Volvo Car Corporation and the department of Electrical Engineering at Chalmers University of Technology.

I would like to express my sincerely gratitude and appreciation to my supervisor, PhD, Andreas Andersson and my examiner, Prof. Torbjörn Thiringer, for those great ideas, close guidance and support along the way. I also want to thank my friends Junfei Tang, Zhenghua Zhang and Wenhao Zhang for their valuable discussions.

Also, I would like to express my deepest love to my parents for supporting me studying abroad. Sweden and Switzerland, Chalmers and ETHz, two years. It has been a great ride.

<div align="right">Yangdi He, Gothenburg, September 2018</div>

Contents

1

Introduction

In this chapter, the background knowledge is briefly stated first. The purpose of the thesis is then stated, followed by the outline of this thesis work.

1.1 Background

The electric machine is a key part in an electric vehicle (EV). Permanent magnet synchronous machine (PMSM) is widely used in an EV due to its high efficiency and high power density which are crucial characteristics. To design a high-performance PMSM system is highly necessary for an EV. Much attention in the previous work has been paid to the performance of the motors themselves, with relatively little consideration to the influence of the power converters in the system. A voltage source inverter (VSI) is typically used in a PMSM system for DC to AC electric energy conversion. The inverter performance is greatly affected by the selection of modulation techniques. As a result, the switching and conduction losses of the power transistors, the output current linearity, the converter efficiency are key factors in the system performance evaluation[1].

In a VSI, the conversion of DC to three-phase AC is exclusively done in the switched mode using different modulation strategies. Over the years, several PWM techniques have been developed and they can be classified into continuous PWM (CPWM) and discontinuous PWM (DPWM). For CPWM, the modulating signal is a continuous time varying signal, including sinusoidal PWM (SPWM), space vector modulation (SVM) and third-harmonic injection PWM (THIPWM). SVM is capable of increasing the dc-link utilization in the linear region by 15 % compared to SPWM. DPWM also provides the same linear range of modulation index as SVM, but by utilizing a discontinuous modulating signal, DPWM reduces switching losses and improves inverter efficiency, at the expense of higher harmonics in the output waveform[2]. As DPWM reduced the turn-on and turn-off times of transistors, which makes it possible to further increase the switching frequency, switching losses can be reduced for DPWM methods. The conduction losses are barely influenced by PWM methods[3]. In some other related work[4][5], the control of PWM inverters in the over-modulation range including the six-step mode is investigated. Moreover, the application for a three-level NPC inverter using SVM algorithm is also discussed in [6][7].

1.2 Goal

The goal of this thesis work is to implement different modulation techniques into the existing PMSM control system to compare the resulting key parameters and performances such as current THD and inverter losses. Preferably, based on different criteria, a favorable method can be found in different operation regions of the speed-torque maps. Thus, a combination of different modulation techniques can enhance the performance to a large extent.

1.3 Outline

In Chapter 2, a brief introduction to the current simulation system as well as an initial parameter table will be made. In Chapter 3, the principle of different modulation strategies is explained in details. MTPA is discussed and the calculation of harmonics and losses are presented. Driving cycles are also introduced as a practical way of evaluating the system performance. In Chapter 4, all the modulation methods discussed before are implemented into the control system and the waveforms are shown. In Chapter 5, simulation results of different parameters from different modulation methods are presented in speed-torque maps. Those map plots are compared and analyzed in details. Driving cycle evaluation and some line plots based on different switching frequencies are made as well. The conclusion is finally drawn in Chapter 6.

2

Case Setup

In this chapter, the main structure of the provided PMSM drive system will be presented. The initial parameter setting of the machine and the inverter will also be illustrated.

2.1 Electric drive system

The structure of the existing PMSM field-oriented control system is shown in Fig. 2.1. The field-oriented control part consists of a PI speed controller, MTPA calculation, a PI current controller with anti-windup and a PWM modulator. The reference voltages are sent into the inverter and then comes the PMSM model, which features the S-function. The detailed MTPA principle will be discusses in Chapter 3.2.1.
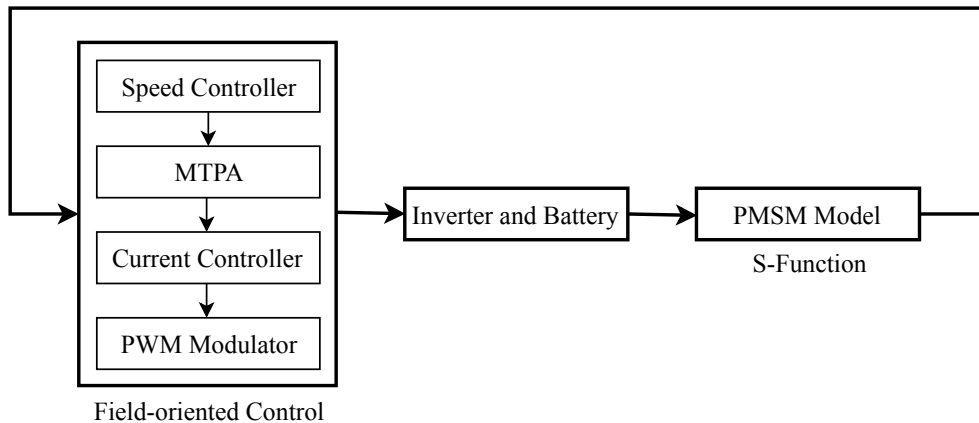
Figure 2.1: Structure of the drive system

2.2 Initial parameters

The parameters of the machine and the inverter are shown in Tab. 2.1 and Tab. 2.2.

Table 2.1: PMSM PARAMETERS

Variable	Value
R_s	0.0132 [Ω]
L_d	0.193 [mH]
L_q	0.447 [mH]
Ψ_m	0.048 [Wb]
J	0.0813 [$kg \cdot m^2$]
p	5
$I_{rms,max}$	150 [A]
n_{max}	8000 [rpm]

Table 2.2: INVERTER PARAMETERS

Variable	Value
V_{dc}	240 [V]
f_{sw}	10 [kHz]

3

Theory

In the first part of the theory, the fundamental knowledge of several modulation strategies will be introduced. In the second part, multiple performance evaluation methods will be applied to make a comparison of the modulation techniques from difference angles.

3.1 Modulation strategies

Sinusoidal pulse width modulation (SPWM) is a method of pulse width modulation used in inverters. An inverter produces an AC output voltage from a DC link by using transistors such as the IGBT. By comparing the reference analog signal with a high-frequency carrier waveform, the fundamental of the output digital signal will appear as a sinusoidal wave. However, the drawback is that the DC voltage utilization is relatively low. Also, the SPWM does not have the freedom to position zero space vectors, which is going to be discussed in the following chapters. Thus, SPWM is not going to be further investigated in this thesis. Next, three main types of modulation strategies including third-harmonic injection PWM (THIPWM), space vector modulation (SVM) and discontinuous PWM (DPWM) will be introduced in details.

3.1.1 THIPWM

The range of linear modulation of a three-phase inverter can be increased by adding a common-mode third-harmonic signal into the reference waveform of each phase. This third-harmonic component will not affect the line-to-line fundamental output voltage, as the common mode voltages cancel each other between the phases. However, it does reduce the peak value of phase voltages which will be demonstrated in Chapter 3.1.1.1. Hence, the modulation index can be increased beyond unity without moving into over-modulation, i.e., the region where the reference magnitude exceeds the peak of the carrier waveform during the fundamental cycle. Therefore THIPWM will extend the linear modulation range by 15 % extra. Over-modulation produces low-frequency base-band distortion and is favorable to be avoided[8]. One-sixth (1/6) and one-quarter (1/4) THIPWM will be discussed, differentiated by the amplitude of the injected common-mode component.

3.1.1.1 1/6 THIPWM

When injecting a sinusoidal third harmonic signal, the optimum amplitude of third harmonic component is to be considered. The highest DC bus utilization can be

obtained when the third harmonic component brings down the resulting waveform's peak amplitude the most. Consider a simple fundamental sinusoidal wave along with a third harmonic of an unknown amplitude, x. Consider x as a parameter and θ as the unknown variable first,

$$F(\theta) = sin(\theta) + xsin(3\theta) \tag{3.1}$$

Then, finding the extreme of the above function using $dF(\theta)/d\theta = 0$ gives[9]

$$\theta = cos^{-1}\left(\sqrt{\frac{9x-1}{12x}}\right) \tag{3.2}$$

Substituting θ in (3.1) with (3.2) and rewriting the equation gives[9]

$$G(x) = (3x+1)\sqrt{\frac{3x+1}{12x}} - 4x\left(\frac{3x+1}{12x}\right)^{\frac{3}{2}} \tag{3.3}$$

Taking the derivative of x in (3.3) to find the extreme of $G(x)$ gives two solutions for x, -1/3 and 1/6. After doing second order derivative, it turns out that function $F(\theta)$ reaches the maximum and the function $G(x)$ reaches the minimum when $x = 1/6$ and $\theta = 60$ correspondingly [9]. In other words, when the amplitude of the third harmonic component is 1/6 of the amplitude of fundamental, the peak of the resulting signal is the lowest with a relatively highest RMS value. The best DC bus utilization is achieved. Substituting $x = 1/6$ and $\theta = 60$ in (3.1) gives the peak value, 0.866. This gives a modulation factor of $1/0.866 = 1.1547$, leading to a higher DC bus utilization. The waveform is shown in Fig. 3.1.
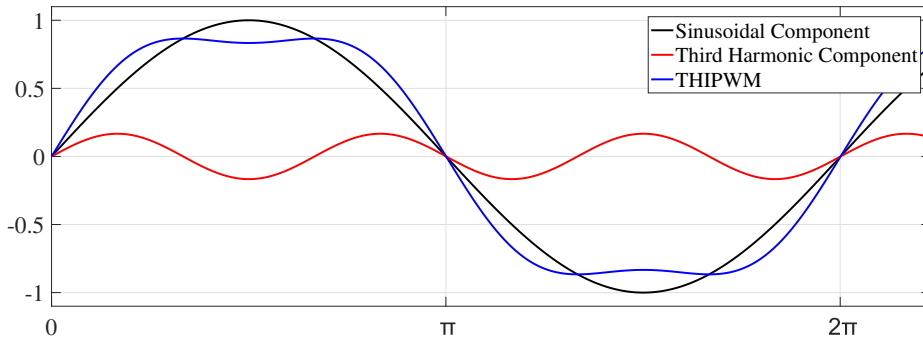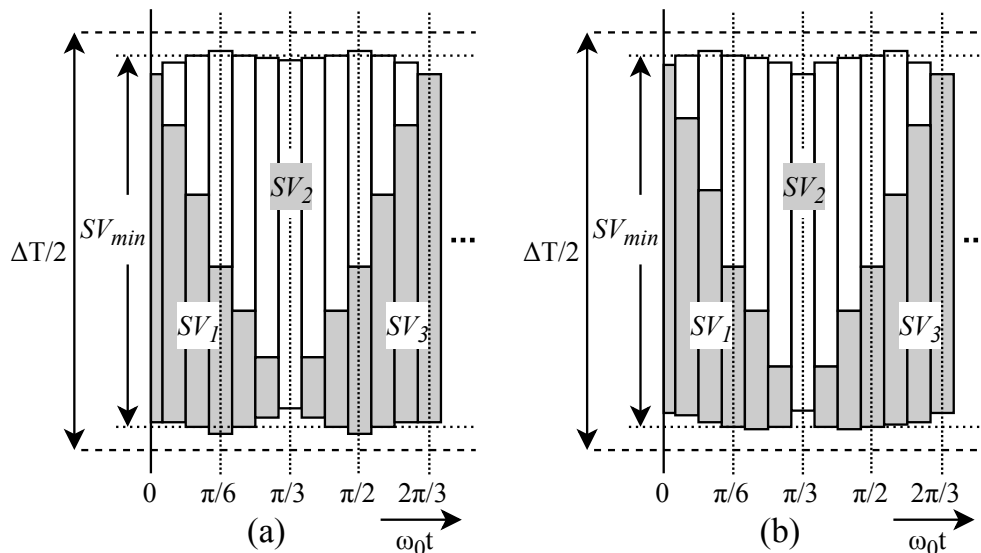

**Figure 3.1:** One-sixth sinusoidal THIPWM

3.1.1.2 1/4 THIPWM

For conventional one-sixth THIPWM, only at $\pi/6$ and $\pi/2$ in the fundamental phase angle, the total active space vector period is identically placed in the center of the half carrier period. However, one-quarter THIPWM centers the total active space vector interval at every $\pi/6$ step and also offsets the total interval slightly outside the SV_{min} region in between, where SV_{min} is the limiting factor for the maximum possible modulation index of M = 1.15. In other words, the main difference is whether it is centered at $\pi/3$ and $2\pi/3$ or not, which is shown in Fig. 3.2. Thus, the

harmonic performance of one-quarter THIPWM is improved due to better asymmetry and equal division of zero vectors, although there is some minor losses due to the fact that some space vectors are placed slightly outside of the SV_{min} region[8]. The waveform is shown in Fig. 3.3.

Figure 3.2: Space vector placement for (a) PWM + one-sixth magnitude third-harmonic (b) PWM + one-quarter magnitude third-harmonic
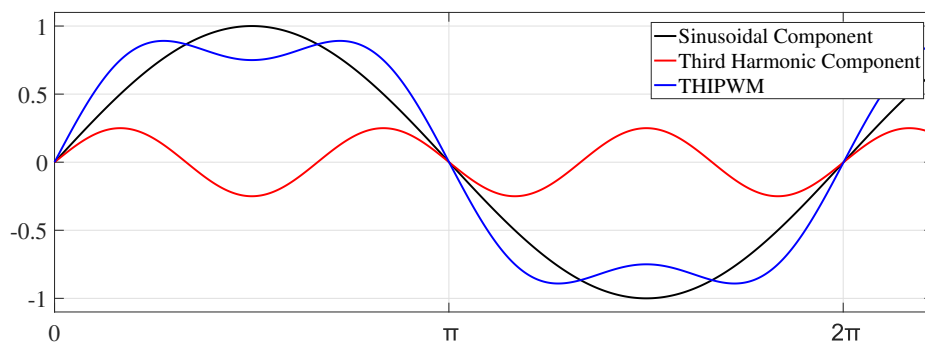
**Figure 3.3:** One-quarter sinusoidal THIPWM

3.1.2 SVM

As pulse placement within each half period of the carrier has a significant effect on both the maximum output voltage of a voltage source inverter and the harmonic behaviour of the modulation implementation, space vector modulation (SVM) is introduced which simply manipulates the placement of the inactive intervals within each half period and can offer advantages over carrier-based PWM in terms of performance, ease of implementation, and maximum modulation index[8].

SVM is introduced based on the fact that there are only eight possible switching states for a three-phase inverter, as is shown in Fig. 3.4. Among these, two states (SV0, SV7) correspond to a short circuit at the output, while the other six can be considered reasonable to establish space vectors in the d-q complex plane, as shown in Fig. 3.5. Each space vector corresponds to a particular angular position. The magnitude of the vectors can be calculated from

$$V_m = \frac{2}{3}V_{dc} \tag{3.4}$$

where V_{dc} is the DC bus voltage.
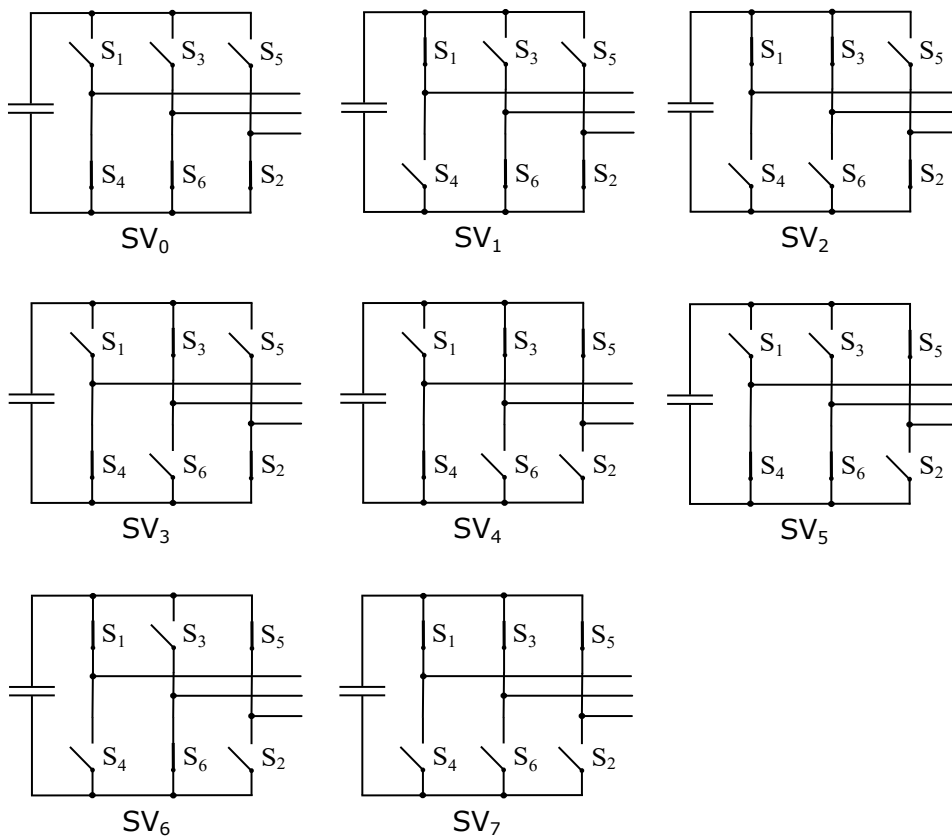
Figure 3.4: Eight possible switching combinations of a 3-phase VSI
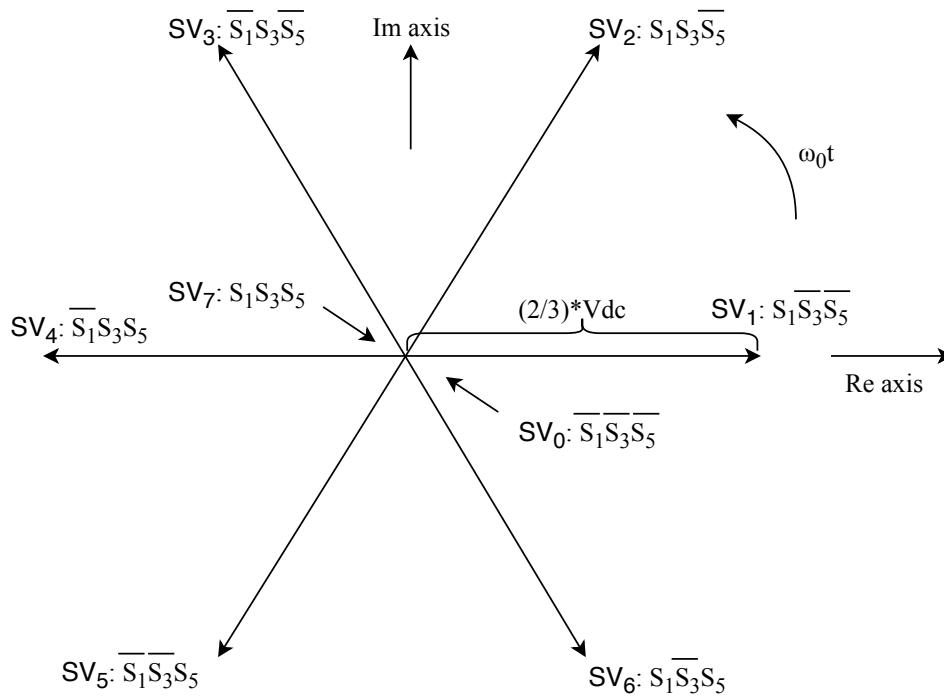
Figure 3.5: Eight possible voltage vectors in d-q plane

At any time, an arbitrary output voltage vector V_0 follows as a consequence of the summation of a number of fundamental space vectors within half of a switching period $\Delta T/2$. This is shown in Fig. 3.6 where the reference voltage vector is in the first $60°$ segment of the plane for example.
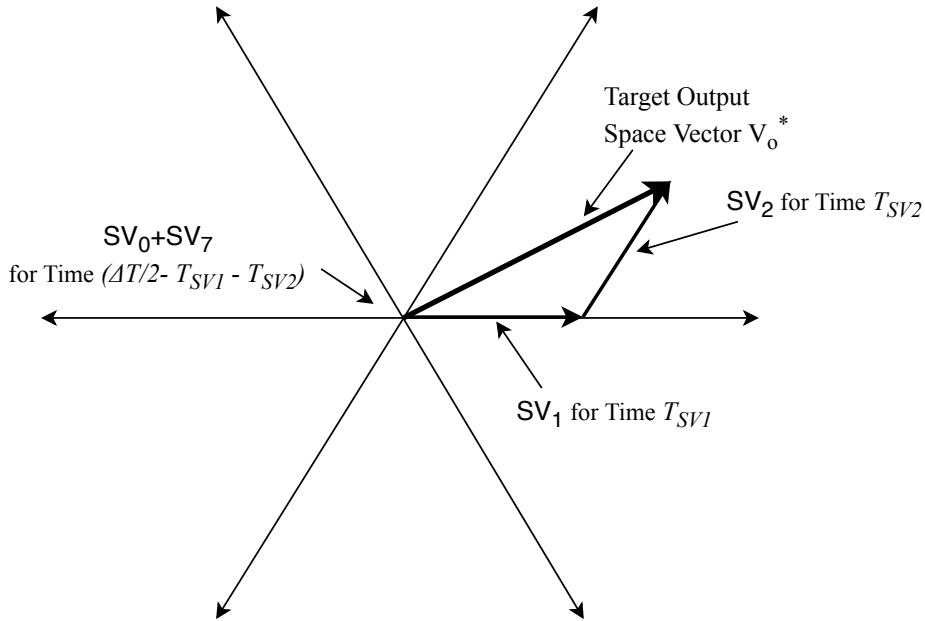
Figure 3.6: An arbitrary voltage vector can be formed by two nearest space vectors.

Unlike SPWM where the position of these zero vectors are predetermined by the algorithm and there is no opportunity for variation, for SVM and DPWM which will be introduced later, the zero space vector positions are undefined and thus there is freedom to explore possible harmonic benefits by manipulating the zero space vector placements within each half period of the carrier. The typical SVM implementation centers the active space vectors in each half carrier period and splits the remaining zero space vector between SV_0 and SV_7 time equally. Taking the first 60° segment for example, this creates a space vector sequence of

$$SV_0 \rightarrow SV_1 \rightarrow SV_2 \rightarrow SV_7 \rightarrow SV_7 \rightarrow SV_2 \rightarrow SV_1 \rightarrow SV_0 \qquad (3.5)$$

Figure 3.7 shows the pulse pattern in the first sector for SVM with equally spaced zero space vectors, SV_0 and SV_7. The sequence of space vectors reverses over a complete carrier period in order to reduce harmonics by maintaining symmetry. For the other sectors, all the combinations are shown in Fig. 3.8. Furthermore, SVM can be easily implemented using the triangle comparison approach shown in Fig. 3.9, because SVM features equal division of null vector time (zero vectors) and the triangular THIPWM injects a common mode component which equals to $(V_{max} + V_{min})/2$, where V_{max} and V_{min} are the maximum and minimum value of the three phase reference voltages. They have an equivalent effect and will generate the same results. The detailed implementation of SVM will be shown in Chapter 4.2. Instead of equal division of zero vectors, DPWM features alternative zero vector placement which will be discussed in the following chapters.
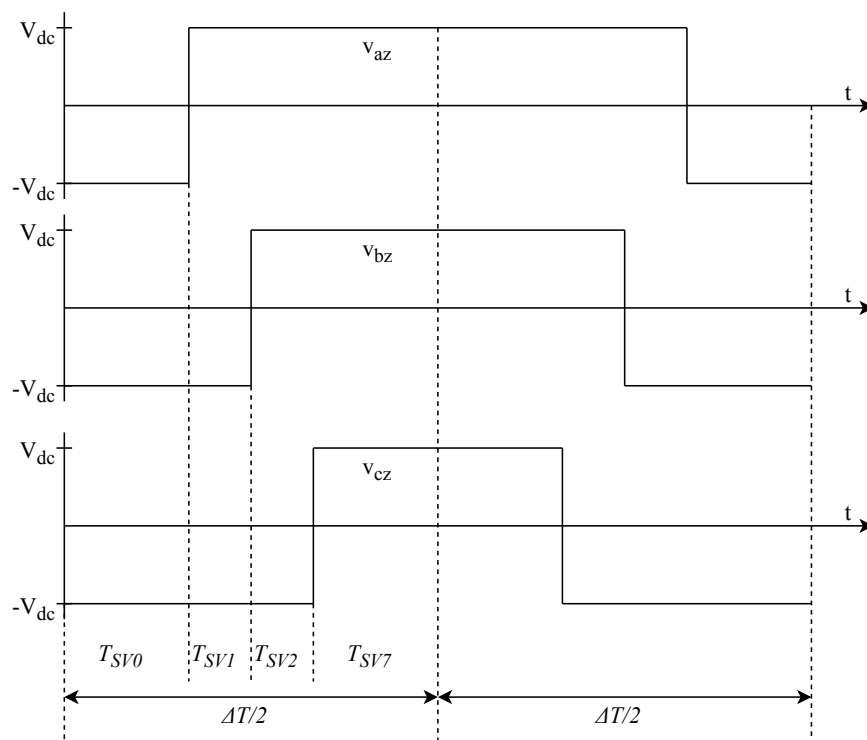
Figure 3.7: Pulse pattern of space vector modulation in the first sector with centered active space vectors.
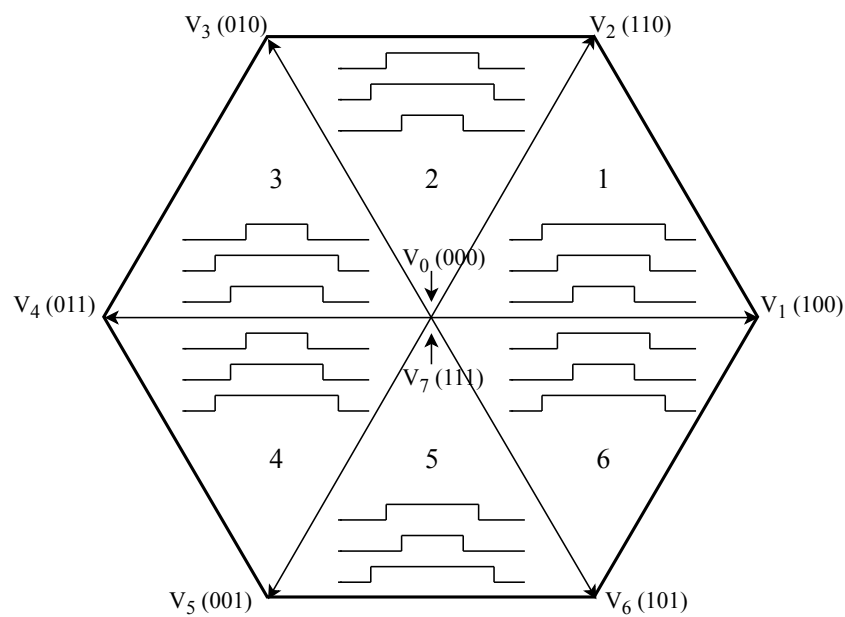
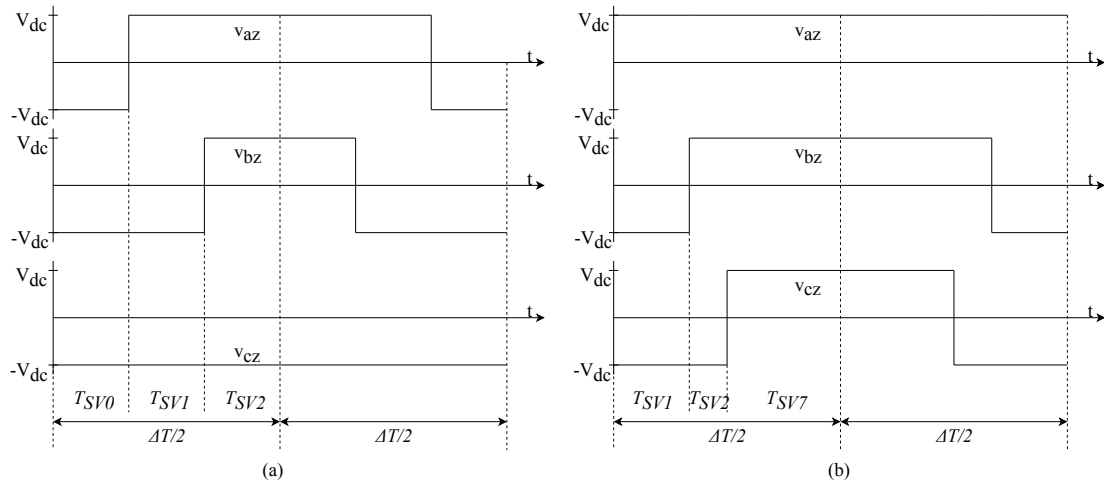**Figure 3.8:** All SVM switching combinations
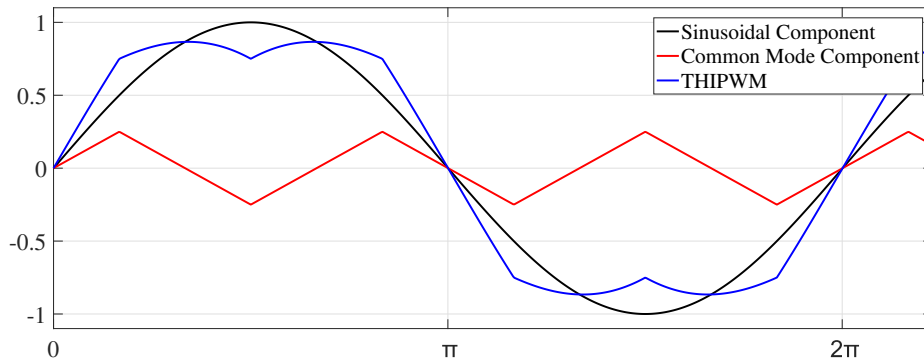
Figure 3.9: Triangular THIPWM

3.1.3 DPWM

When the active space vectors in successive half carrier intervals are joint together, the intermediate zero vector will disappear consequently, i.e., a discontinuous mode of SVM, DPWM. DPWM has the advantage of eliminating one switching transition in each half carrier interval, which allows the switching frequency of the converter to increase by a nominal value of 3/2 with the inverter losses unchanged. Thus, lower switching losses and higher inverter efficiency can be expected compared to continuous PWM. However, asymmetry will bring about more harmonics at the same time. 120° DPWM, 60° DPWM and 30° DPWM, differentiated by how long one phase is clamped to +/- DC successively, will be introduced next.

3.1.3.1   120° DPWM: DPWMMAX, DPWMMIN

The most straightforward approach is to remove one of the two zero space vectors, SV0 or SV7. Each phase leg is now continuously locked to DC link voltage, either +Vdc or -Vdc, for one-third of the complete period (120°). This is termed 120° discontinuous PWM (DPWM). DPWMMIN and DPWMMAX are corresponding to plus and minus DC clamping. The pulse patterns are shown in Fig. 3.10. The switching combinations (half period) are presented in Fig. 3.11. Line-to-line voltages become asymmetrical and result in worse harmonic performance compared to continuous PWM. However, as mentioned before, less switching means lower switching losses. Moreover, another disadvantage is that conduction losses are not distributed equally across the two transistors in each phase leg. To solve this problem, 60° and 30° DPWM clamping will be introduced next as it clamps to +/- DC voltage alternatively in each half period.
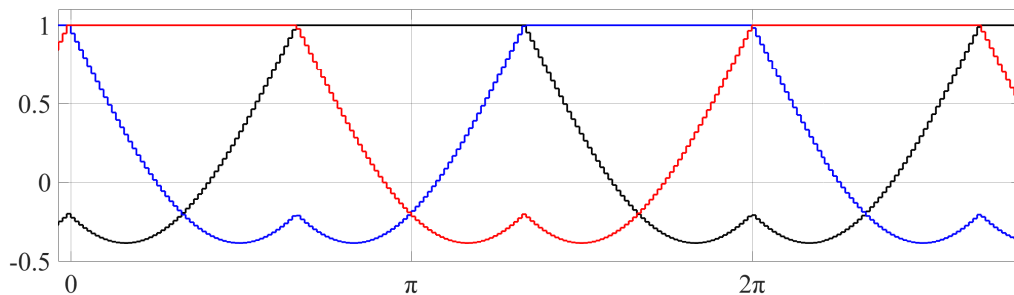
Figure 3.10: (a) Pulse pattern of DPWMMIN in the first sector with centered active space vectors. (b) Pulse pattern of DPWMMAX in the first sector with centered active space vectors.
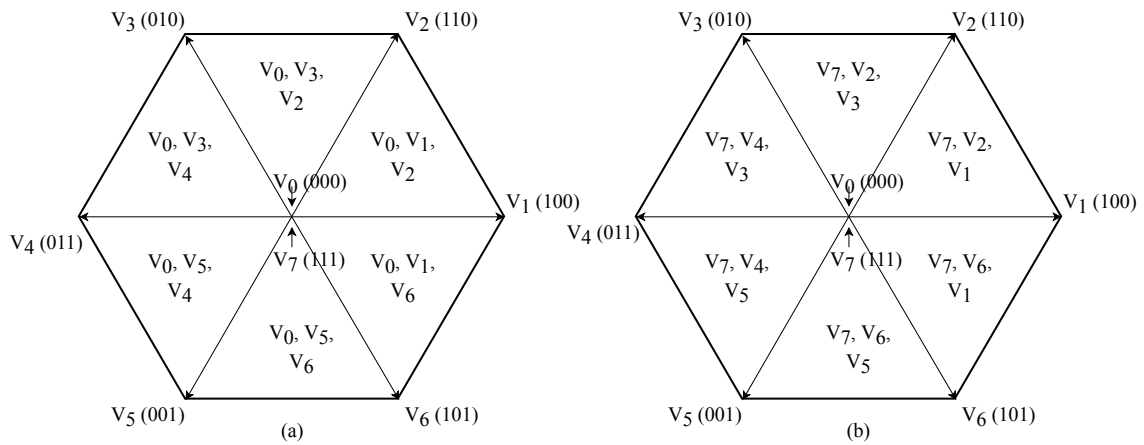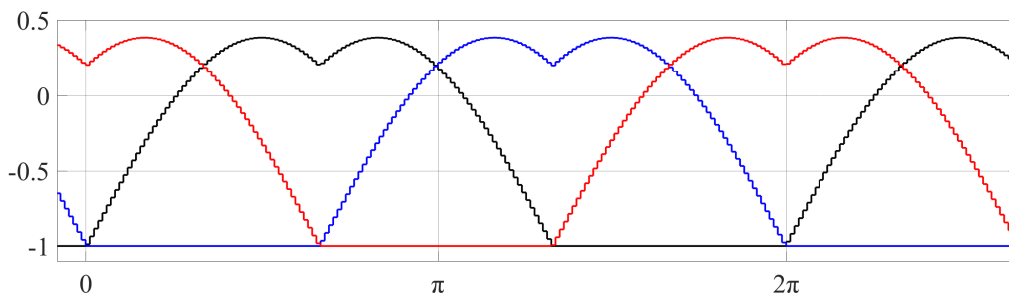

Figure 3.11: (a) DPWMMIN switching combinations in a half period (b) DPWMMAX switching combinations in a half period

The modulation patterns are shown as below.

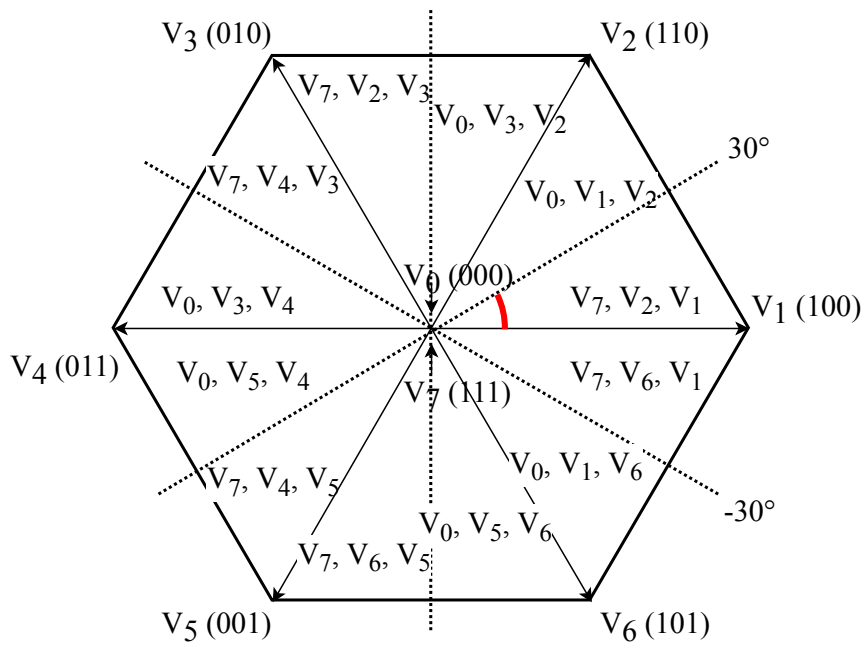**Figure 3.12:** Modulation waveform of DPWMMAX

13

Figure 3.13: Modulation waveform of DPWMMIN

3.1.3.2   60° DPWM: DPWM1, DPWM0, DPWM2

An improved modulation strategy is to place the space vectors to eliminate zero space vectors SV0 and SV7 alternately for successive 60° period. It is called 60° discontinuous modulation as each phase leg is now clamped to +/- DC for only 60° at a time. The resulting advantage is that the line-to-line voltage is now symmetrical. The typical type of 60° DPWM is termed DPWM1. It centers the non-switching periods for each phase leg symmetrically around the fundamental voltage's positive and negative peaks. This is optimal for a resistive load, since the peak of the line current is synchronized with the peak of the fundamental voltage. Therefore, each phase leg does not switch when the current is at its peak value, which minimizes switching losses of the transistors[8].

Instead of zero clamping at voltage peak, it is feasible to place each 60° non-switching interval anywhere within the 120° where the corresponding phase reference voltage is the maximum/minimum among the three phases. In other words, there is freedom of 60° to rearrange the switching. For a lagging power factor load, it is preferable to retard the non-switching interval by up to 30° lag (DPWM2). For a leading power factor load, it is preferable to advance the non-switching interval by up to 30° lead (DPWM0). However, this modulation technique re-introduces asymmetry into the line-to-line voltage.

The switching combinations of DPWM1 are shown in Fig. 3.14. For example, in this case, from -30° to 30°, one phase leg is clamped to +Vdc. The angle marked red is flexible to range from 0° to 60°, which refers to phase shift clamping, DPWM0 and DPWM2.
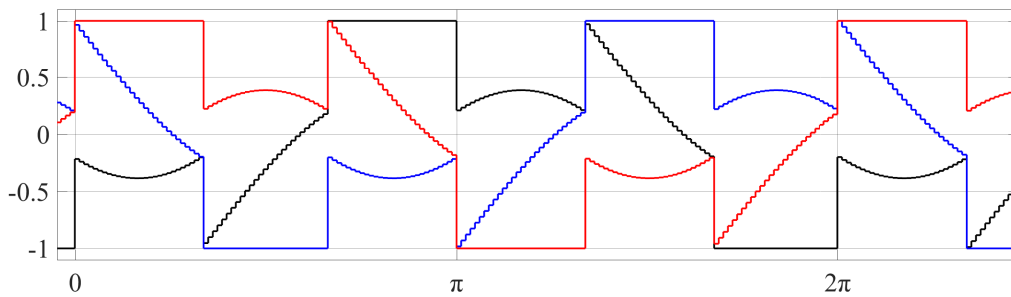
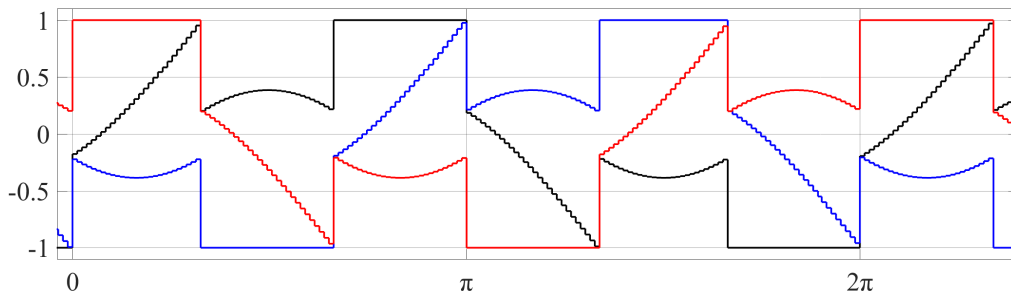**Figure 3.14:** DPWM1 switching combinations

The modulation patterns are shown as below.
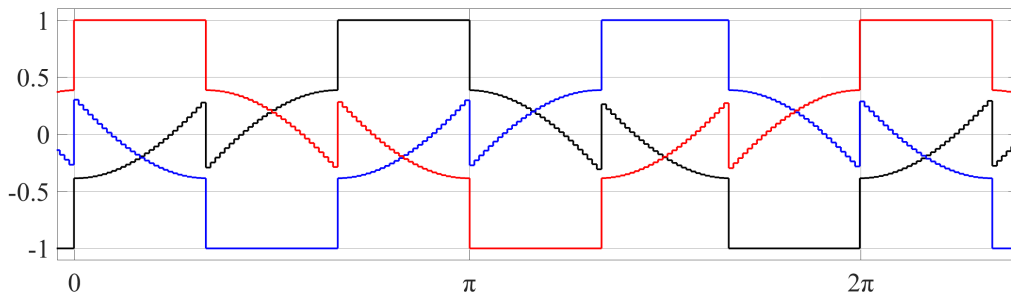
Figure 3.15: Modulation waveform of DPWM1

Figure 3.16: Modulation waveform of DPWM0

Figure 3.17: Modulation waveform of DPWM2

3.1.3.3 30° DPWM: DPWM3

30° discontinuous modulation, i.e., DPWM3, requires each phase leg to clamp for only every 30°. Figure 3.18 shows the switching combinations for this modulation strategy and the line-to-line voltage is again symmetrical.

Figure 3.18: DPWM3 switching combinations

The modulation pattern is shown as below.

Figure 3.19: Modulation waveform of DPWM3

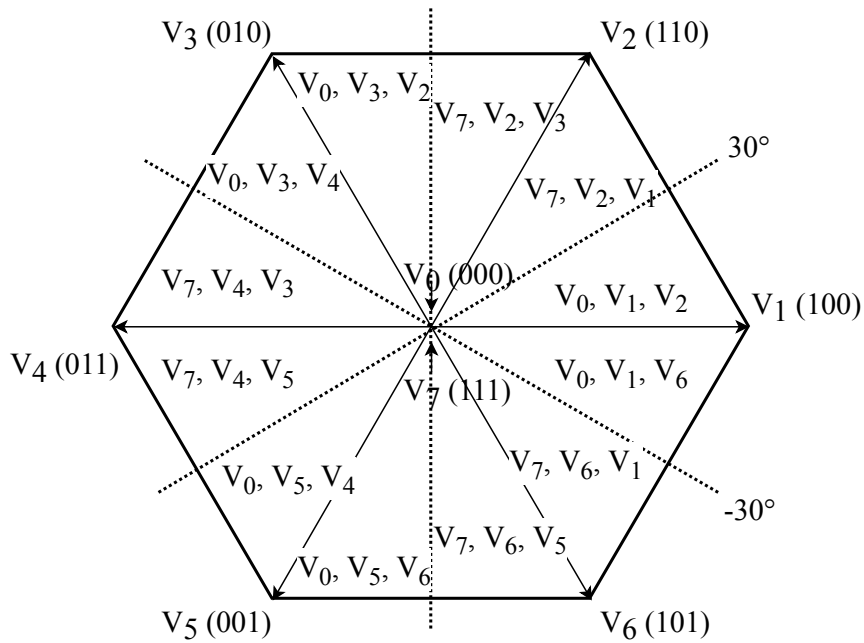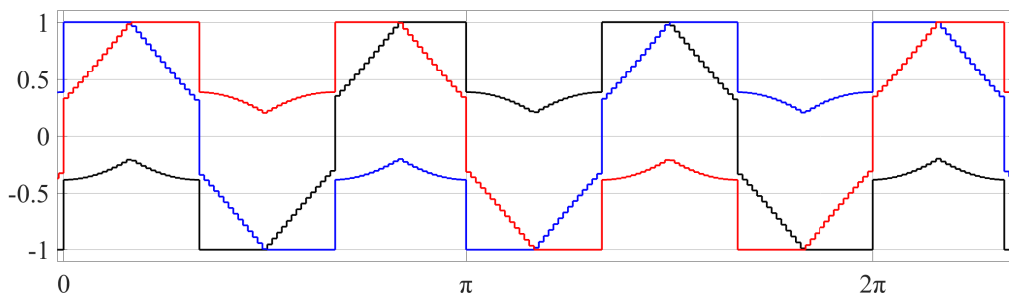From previous subchapters, it was shown that the third-harmonic injection method and SVM achieve the same space vector placement essentially. DPWM and SVM only differ in the zero space vector placement as DPWM is achieved by eliminating selected zero space vectors for sections of the fundamental cycle, and the resulting different switching combinations lead to significantly different modulation waveforms. DPWM results in lower switching losses of transistors, higher inverter efficiency and higher current THD, which will be validated in the results chapter.

3.2 Performance evaluations

Apart from the knowledge of modulation strategies as introduced above, some key parameters which can be used to evaluate the PMSM system will be demonstrated next. The theory of MTPA will first be introduced. Harmonic analysis, conduction and switching losses of IGBT will then be analyzed. Finally, driving cycle will also be involved as a way of evaluating the machine performance.

3.2.1 MTPA

Electromagnetic torque of a PMSM can be calculated as

$$T = \frac{3}{2}n_p \left(\psi_{PM}i_q + (L_d - L_q)i_d i_q\right) \tag{3.6}$$

where n_p is the number of pole pairs. L_d, L_q are d,q inductances. i_d, i_q are d,q currents which are to be solved. ψ_{PM} is the permanent magnet flux constant. d axis is aligned with the magnetic field of the permanent magnet. q axis is 90 degrees (electrical) leading. Due to geometric position of the magnets, $L_d \leq L_q$ for a salient pole machine. The difference between them generates a torque, i.e., reluctance torque. q current is mainly responsible for the torque production. Negative i_d is needed to counteract the permanent magnet flux in order to generate positive torque, i.e., field weakening.

Flux and voltage are coupled through frequency in stationary operation neglecting the stator resistance, and flux has a limitation according to

$$v_1 = j2\pi f_1\psi_1 \Rightarrow \psi_{lim}^2 = min\left(\psi_{max}^2, \frac{|v_{max}|^2}{f_1^2}\right) \tag{3.7}$$

where f_1 is the base frequency. The flux limit is written as a function of current which describes an ellipse,

$$\psi_1^2 = \psi_d^2 + \psi_q^2 = (\psi_{PM} + L_d i_d)^2 + L_q^2 i_q^2 = L_d^2\left(\frac{\psi_{PM}}{L_d} + i_d\right)^2 + L_q^2 i_q^2 \tag{3.8}$$

where $\frac{\psi_{PM}}{L_d} + i_d$ can be defined as the virtual d current, i_{vd}. Now the flux ellipse is derived with semi-axis $\frac{\psi_1}{L_d}$ in d-axis and $\frac{\psi_1}{L_q}$ in q-axis.

Here, the general problem is that we have two unknowns, i_d and i_q, in (3.6), which opens the possibility for optimization. One control method can be maximum torque per ampere (MTPA). Several cases are demonstrated in Fig. 3.20. All of them consist of constant current magnitude circles, constant torque lines and flux limit ellipse as is derived above, as well as a MTPA curve which is marked with black dots. The dashed circle refers to the maximum current limitation and $T_{max} > T_2 > T_1$. The flux limit is determined by the maximum voltage supplied by the inverter. Torque is a function of i_d and i_q, and $i_{max} > i_2 > i_1$. In Fig. 3.20 (a), the loss-optimal operating points are limited by current only and there is no flux limit in this typical case. The goal of MTPA is to find the maximum torque using the same amount of current. In other words, in order to produce the same torque, the current is to be minimized to reduce I^2R, i.e., copper loss, as much as possible. Among various d-q current combinations, the MTPA curve only consists of working points where the constant torque lines touch the constant current magnitude circles. Following this MTPA curve, maximum torque is acquired with minimum current magnitude within the voltage and current limits. When the maximum voltage limit is reached during field weakening, MTPA is not available any more.
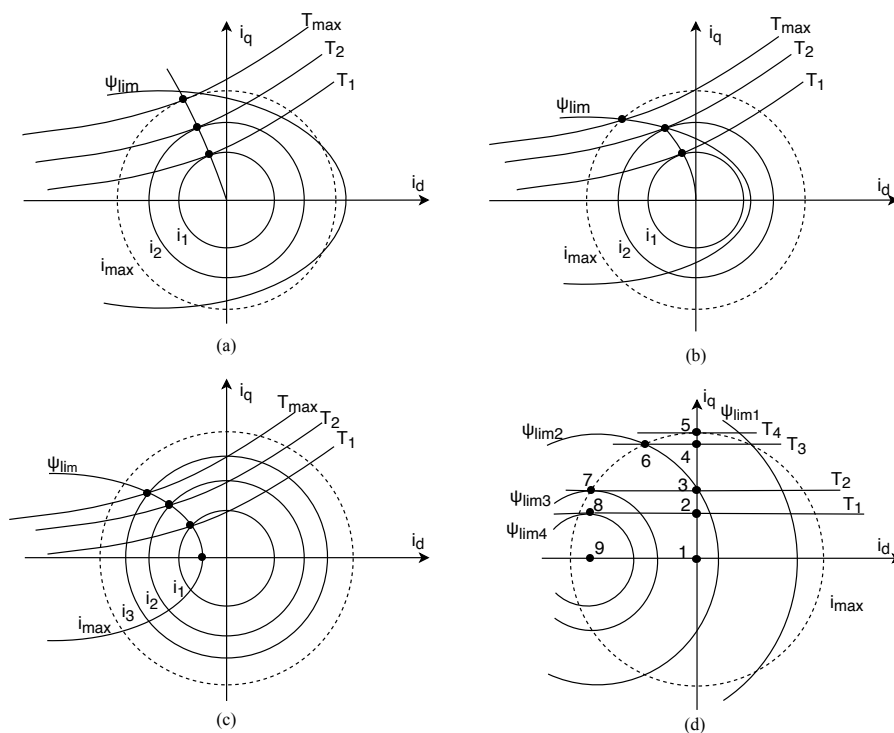
Figure 3.20: (a) MTPA (b) Voltage constrained MTPA (c) MTPV (d) Special case of non-salient machine

In Fig. 3.20 (b), the loss-optimal operating points are limited by both the current and the flux (voltage). As the torque requested increases to a certain extent, the touch point of constant torque line and constant current circle is outside of the voltage limit ellipse and thus cannot be realized. As a result, the possible solutions will fall on the voltage ellipse as torque increases.

In Fig. 3.20 (c), the loss-optimal operating points are limited by flux only and there is no current limit. In this case, it is impossible to work on the touch point of constant torque line and constant current circle. Note that in this figure, it is an infinite speed machine where the center of the flux ellipse is inside the max current circle and the infinite speed can be achieved.

In Fig. 3.20 (d), the special case of non-salient machine is considered, i.e., $L_d = L_q$. As a result, the constant torque line will become horizontal lines and flux limit ellipses will turn into circles according to (3.6) and (3.8) shown above. Since reluctance torque is zero, the torque is proportional to i_q. For point 5 - 7, it is voltage constrained MTPA. For point 8 - 9, it is MTPV. Field weakening takes place from point 5 to 9, where $\psi_{lim1} > \psi_{lim2} > \psi_{lim3} > \psi_{lim4}$. In this figure, as flux ψ_d is further reduced to zero without reaching the maximum current limit, then the machine speed can be increased to infinity theoretically since the back EMF can be reduced to zero, i.e., 'infinite speed machine':

$$i_d = -\frac{\psi_{PM}}{L_d} \tag{3.9}$$

19

Limitations, i.e., stator voltage, stator flux and stator current, may vary with time but for a certain moment they are fixed as follows. They are implemented in the MTPA algorithm. The maximum stator flux is set to prevent demagnetizing the permanent magnet, which is normally covered in the machine design.

$$v_1^2 = v_d^2 + v_q^2 \leq v_{max}^2 \tag{3.10}$$

$$\psi_1^2 = \psi_d^2 + \psi_q^2 \leq \psi_{max}^2 \tag{3.11}$$

$$i_1^2 = i_d^2 + i_q^2 \leq i_{max}^2 \tag{3.12}$$

where v_1, ψ_1 and i_1 refers to stator voltage, flux and current. They are all represented in d,q components and have certain maximum limitations, i.e., v_{max}, ψ_{max} and i_{max}. In the base speed range from standstill to rated speed, the stator flux and the stator current are the relevant limitations. While in the field weakening range above the rated speed, the stator voltage and the stator current are the limiting quantities. Since the maximum voltage must not be exceeded, the flux must be reduced at high speeds. Since the flux is produced by the permanent magnet, its effect must be compensated by injecting a negative current in the d-axis.

Based on the theory above, in the given MTPA algorithm, the envelope is solved first: for each speed, as the machine works in an nonlinear fashion, different combinations of i_d and i_q are tried out to reach the maximum torque based on MTPA, while the limitations above must be met. When speed is higher than base speed, the working points where voltage is larger than v_{max} will be filtered out. Next, in the interior area, for each speed and given torque, MTPA rule is used again for selection. In the field weakening region, the working point closest to the tangency point on the flux limit ellipse is selected. During the whole calculation process, iterations are used to approach the final solution and vectorization helps Matlab calculate faster. The d,q inductance is varying considering saturation.

3.2.2 Harmonic analysis

Two ways of evaluating harmonic performance are considered.
First, the manual FFT and THD calculation is conducted based on

$$THD = \frac{\sqrt{h_1^2 + h_2^2 + h_3^2 + ... + h_n^2}}{f_1} \tag{3.13}$$

where h_1 is the first harmonic and f_1 is the fundamental component. The manual calculation takes all inter-harmonics into consideration. One example of the generated harmonic spectrum is shown in Fig. 3.21 when the speed reference is 2000rpm and torque is 40Nm.
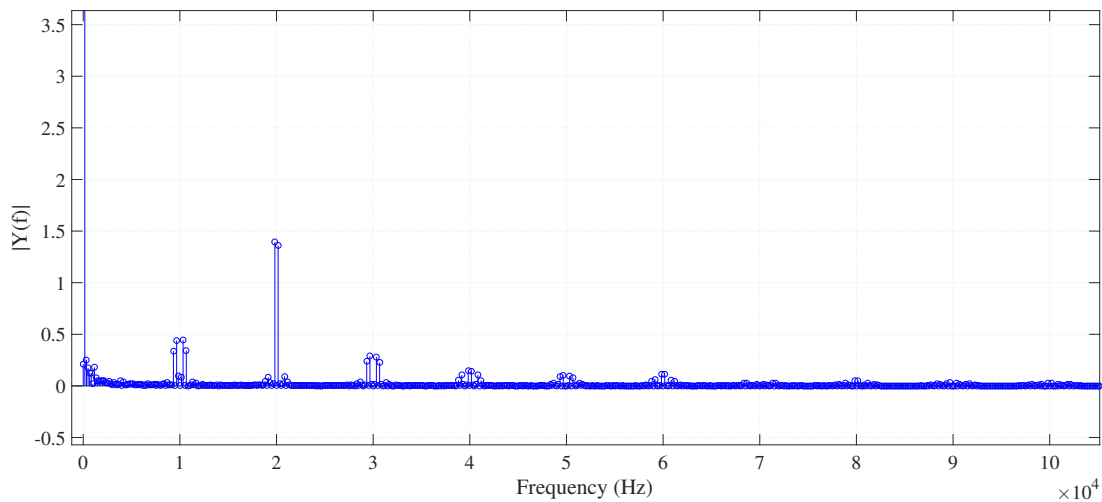
Figure 3.21: Example spectrum generated from manual FFT

The other way is to use the Matlab Powergui toolbox to generate THD automatically providing specific fundamental frequency and other parameters such as start time, number of cycles and max frequency. Next, the results from the toolbox can be extracted in the structure manner and then be used in the final mapping script. The harmonic spectrum is also shown in the Powergui window.

The results of these two methods are the same if taking the same start time and number of cycles for calculation. The Powergui method is selected for all of the following investigations.

Furthermore, TDD (total demand distortion) for current is defined as

$$TDD = \frac{\sqrt{i_1^2 + i_2^2 + i_3^2 + ... + i_n^2}}{i_L} \tag{3.14}$$

where i_L is maximum demand load current which is maximum phase current in this case. As low torque leads to a low current which means relatively high harmonic components, the THD in the low-torque region could be very high and make the THD map hard to scale in this region. TDD is thus introduced to remove the huge gap between low current and high current regions and make the map plot look smooth and close to unity.

3.2.3 Losses of semiconductor devices

Both conduction losses and switching losses are considered for each transistor in a 3-phase inverter. The related calculations are as follows.

3.2.3.1 Conduction losses

The conduction loss of an IGBT occur when it is conducting. The average power dissipation during conduction in one switching period can be written as

$$P_{cond} = \frac{1}{T_{sw}} \int_0^{T_{sw}} v_{ce,sat} i_{ce} dt \tag{3.15}$$

where T_{sw} is the switching period, $v_{ce,sat}$ is on-state voltage, i_{ce} is on-state current. $v_{ce,sat}$ can be further expresses as

$$v_{ce,sat} = v_{ce,0} + r_{on} i_{ce} \tag{3.16}$$

where $V_{ce,0}$ is the saturation voltage at zero current and r_{on} is the on-state resistance of IGBT. Both parameters can be found in IGBT datasheet.

Then the conduction loss of IGBT can be formulated as

$$
\begin{aligned}
P_{cond,IGBT} &= \frac{1}{T_{sw}} \int_0^{T_{sw}} (v_{ce,0} + r_{on} i_{ce}) i_{ce} dt \\
&= v_{ce,0} I_{ce,avg} + r_{on} I_{ce,rms}^2
\end{aligned}
\tag{3.17}
$$

where $I_{ce,avg}$ is the average value and $I_{ce,rms}$ is the RMS value of the on-state current.

For the conduction loss of the parallel diode, the formula is similarly derived as

$$P_{cond,diode} = v_{F,0} I_{d,avg} + r_F I_{d,rms}^2 \tag{3.18}$$

where $I_{d,avg}$ is average value and $I_{d,rms}$ is RMS value of the on-state current through the diode. $v_{F,0}$ and r_F can be found in IGBT module datasheet.

For a three-phase AC motor drive system, the topology is shown in Fig. 3.22.
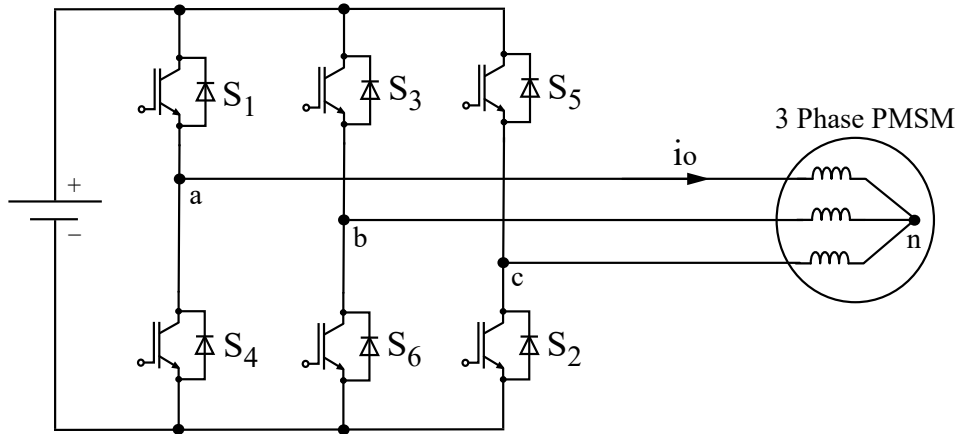
Figure 3.22: Three-phase AC motor drive

IGBT conduction loss:

$$
\begin{aligned}
P_{cond,IGBT} &= v_{ce,0} I_{ce,avg} + r_{on} I_{ce,rms}^2 \\
&= v_{ce,0} I_0 \left(\frac{1}{2\pi} + \frac{m_a cos\alpha}{8}\right) + r_{on} I_0^2 \left(\frac{1}{8} + \frac{m_a cos\alpha}{3\pi}\right)
\end{aligned}
\tag{3.19}
$$

where $I_0 = \sqrt{2}I_{0,rms}$, $I_{0,rms}$ is the rms value of the output current. m_a is modulation index. The angle α is the phase shift between phase current and voltage and it can be calculated using zero-crossing detection in a Matlab script[10].

Diode conduction loss:

$$
\begin{aligned}
P_{cond,diode} &= v_{F,0}I_{d,avg} + r_F I_{d,rms}^2 \\
&= v_{F,0}I_0(\frac{1}{2\pi} - \frac{m_a cos\alpha}{8}) + r_F I_0^2(\frac{1}{8} - \frac{m_a cos\alpha}{3\pi})
\end{aligned} \tag{3.20}
$$

The overall loss of the three-phase VSI:

$$
P_{cond} = (P_{cond,IGBT} + P_{cond,diode}) * 6 \tag{3.21}
$$

3.2.3.2   Switching losses

The turn-on and turn-off waveforms are considered first for calculating switching losses. When the IGBT turns on, the diode turns off with reverse recovery current taking place. When the IGBT turns off, the diode turns on without losses. Therefore, the total switching losses consist of IGBT turn-on loss, IGBT turn-off loss and diode reverse recovery loss during turn-off.

The switching loss P_{sw} of a three-phase IGBT voltage source converter with sinusoidal AC line current is given by

$$
P_{sw} = \frac{6}{\pi}f_s(E_{ON,I} + E_{OFF,I} + E_{OFF,D})\frac{V_{dc}}{V_{ref}}\frac{\hat{i_L}}{i_{ref}} \tag{3.22}
$$

Here f_s is the switching frequency. $E_{ON,I}$ and $E_{OFF,I}$ are turn-on and turn-off energies of the IGBT respectively. $E_{OFF,D}$ is the turn-off energy of the diode in the IGBT module due to reverse recovery current. V_{dc} is the DC link voltage. $\hat{i_L}$ is the peak value of the AC line current which is assumed to be sinusoidal. The switching energies mentioned above are provided by the datasheet[11] and they are valid under a certain reference voltage V_{ref} and a reference current i_{ref}. V_{ref} is equal to the blocking state voltage of the IGBT before commutation and i_{ref} refers to the on-state current after commutation. They can also be found in datasheet. Equation (3.22) is only valid for continuous PWM since the switching losses become dependent on phase angle for discontinuous PWM[12].

For discontinuous PWM, switching loss calculation for different method is different. Normalize switching loss of discontinuous PWM, $P_{sw_{DPWM}}$ to that of continuous PWM, P_{sw}, where phase angle is independent, as is shown in (3.22). Then the switching loss function (SLF) can be defined as[13]

$$
SLF = \frac{P_{sw_{DPWM}}}{P_{sw}} \tag{3.23}
$$

The SLF function for each DPWM method can be found in [14].

$$SLF = \begin{cases} \dfrac{\sqrt{3}}{2}cos\left(\dfrac{4\pi}{3}+\beta-\theta_s\right) & -\dfrac{\pi}{2} \leq \theta_s \leq -\dfrac{\pi}{2}+\beta \\[3mm] 1-\dfrac{1}{2}sin\left(\dfrac{\pi}{3}+\beta-\theta_s\right) & -\dfrac{\pi}{2}+\beta \leq \theta_s \leq \dfrac{\pi}{6}+\beta \\[3mm] \dfrac{\sqrt{3}}{2}cos\left(\dfrac{\pi}{3}+\beta-\theta_s\right) & \dfrac{\pi}{6}+\beta \leq \theta_s \leq \dfrac{\pi}{2} \end{cases} \qquad (3.24)$$

where θ_s is the load phase shift angle between phase current and voltage. This angle is measured by detecting the zero-crossing of the two signals in a Matlab script and then calculating the phase difference. As the reference voltage in the controller is discrete, the detected zero-crossing time might deviate from the actual zero-crossing time of the fundamental continuous signal. Instead of reconstructing the signal, simple mathematical linearization of the discrete voltage signal is implemented in the Matlab script to acquire the zero-crossing point so that the error is greatly reduced. β is defined as the modulator phase angle increasing from the intersection point of the two reference modulation waves. It simply represents the position shift of the discontinuous state.

In (3.24), by substituting $\beta = 0$, $\beta = \pi/6$ and $\beta = \pi/3$, the SLF functions of DPWM0, DPWM1 and DPWM2 can be derived[13]. The SLF functions of the remaining DPWM methods are given by[13]

$$SLF_{DPWMMAX} = \begin{cases} \dfrac{1}{2}-\dfrac{1}{4}sin\theta_s & -\dfrac{\pi}{2} \leq \theta_s \leq -\dfrac{\pi}{6} \\[3mm] 1-\dfrac{\sqrt{3}}{4}cos\theta_s & -\dfrac{\pi}{6} \leq \theta_s \leq \dfrac{\pi}{6} \\[3mm] \dfrac{1}{2}+\dfrac{1}{4}sin\theta_s & \dfrac{\pi}{6} \leq \theta_s \leq \dfrac{\pi}{2} \end{cases} \qquad (3.25)$$

$$SLF_{DPWMMAX} = SLF_{DPWMMIN} \qquad (3.26)$$

$$SLF_{DPWM3} = \begin{cases} 1+\dfrac{1}{2}(\sqrt{3}-1)sin\theta_s & -\dfrac{\pi}{2} \leq \theta_s \leq -\dfrac{\pi}{3} \\[3mm] \dfrac{1}{2}(cos\theta_s-sin\theta_s) & -\dfrac{\pi}{3} \leq \theta_s \leq -\dfrac{\pi}{6} \\[3mm] 1-\dfrac{1}{2}(\sqrt{3}-1)cos\theta_s & -\dfrac{\pi}{6} \leq \theta_s \leq \dfrac{\pi}{6} \\[3mm] \dfrac{1}{2}(cos\theta_s+sin\theta_s) & \dfrac{\pi}{6} \leq \theta_s \leq \dfrac{\pi}{3} \\[3mm] 1-\dfrac{1}{2}(\sqrt{3}-1)sin\theta_s & \dfrac{\pi}{3} \leq \theta_s \leq \dfrac{\pi}{2} \end{cases} \qquad (3.27)$$

3.2.4   Driving cycles

The combination of the urban driving cycle (ECE) and the extra-urban driving cycle (EUDC) is commonly used for approval testing of emissions and fuel consumption for light duty vehicles in EU. The ECE cycle is designed to represent typical driving conditions of busy European cities and it is characterized by a low engine load, low exhaust gas temperature as well as a maximum speed of 50 km/h. The EUDC cycle is designed to represent more aggressive, high speed driving modes and the maximum speed is 120 km/h while low-powered vehicles are limited to 90 km/h [15]. Parameters such as speed, acceleration and time are included in the data files. Figure 3.23 shows the speed variation of an ECE cycle.
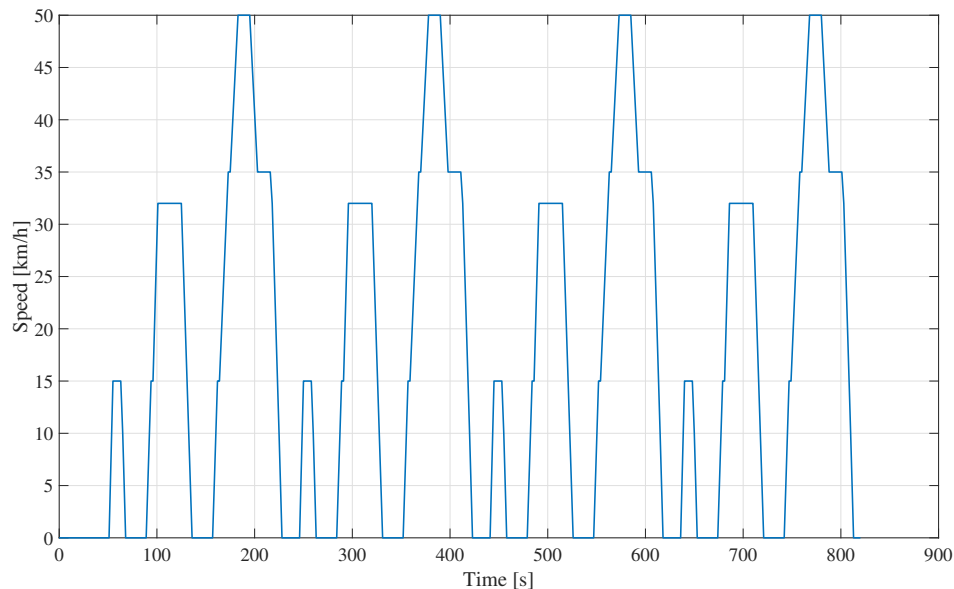
Figure 3.23: Driving cycle ECE - Vehicle speed

Using the QSS Toolbox provided by ETH Zurich, Institute for Dynamic Systems and Control, a Simulink model consisting of a driving cycle module and a vehicle module can be built[16]. In the model, one typical driving cycle is selected and the self-defined vehicle parameters are the input as well. The parameters of the vehicle used in the model is presented in Tab. 3.1. The torque on wheel axis is one of the outputs of the model. Rolling resistance, aerodynamic resistance and inertia are all the forces involved in the calculation for the torque on wheel. After conversion, the torque on the rotor axis is shown in Fig. 3.24.

Table 3.1: VEHICLE PARAMETERS

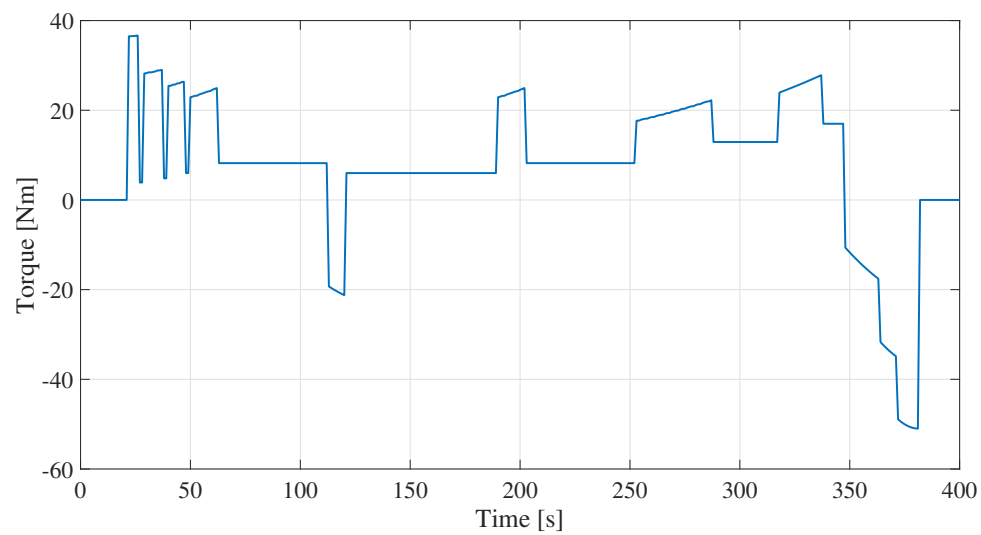| Variable	Value
Total mass of the vehicle	1500 [kg]
Rotating mass	5 [%]
Vehicle cross section	2.8 $[m^2]$
Wheel diameter	0.5 [m]
Drag coefficient	0.29
Rolling friction coefficient	0.01
Gear ratio	10
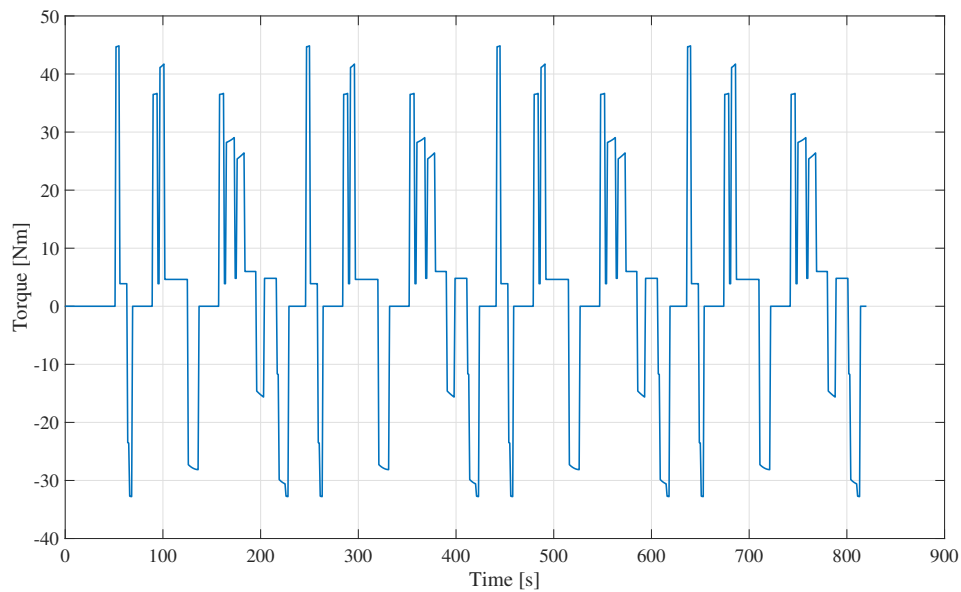
Figure 3.24: Driving cycle ECE - Torque on the rotor axis

Figure 3.25 and 3.26 shows the speed and torque variation of an EUDC cycle.
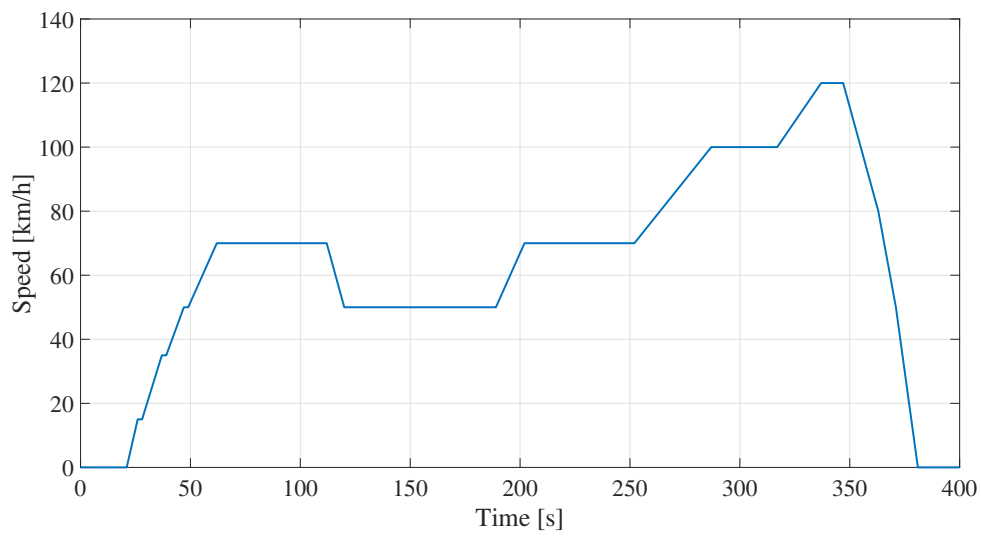
Figure 3.25: Driving cycle EUDC - Vehicle speed

Figure 3.26: Driving cycle EUDC - Torque on the rotor axis

4

Implementation and waveforms

This chapter focuses on how modulation techniques including THIPWM, SVM and DPWM are implemented in the drive system and how the key waveforms behave for each one.

4.1 THIPWM

For 1/6 THIPWM, from the analysis in Chapter 3.1.1.1, the 3-phase reference voltages are given by

$$V_a = 1.15 V_{dq} \left(sin\theta + \frac{1}{6} sin3\theta \right) \tag{4.1}$$

$$V_b = 1.15 V_{dq} \left(sin(\theta - \frac{2\pi}{3}) + \frac{1}{6} sin3\theta \right) \tag{4.2}$$

$$V_c = 1.15 V_{dq} \left(sin(\theta + \frac{2\pi}{3}) + \frac{1}{6} sin3\theta \right) \tag{4.3}$$

where the instantaneous magnitude of the fundamental $V_{dq} = \sqrt{V_d^2 + V_q^2}$ and V_d, V_q are voltages in dq coordinates.

$$sin\theta = \frac{V_a}{V_{dq}} \tag{4.4}$$

$$sin3\theta = 3sin\theta - 4sin^3\theta \tag{4.5}$$

All the equations above are implemented into the Simulink model and Matlab function.

For 1/4 THIPWM, the reference voltages are slightly different as follows and the same method applies.

$$V_a = 1.15 V_{dq} \left(sin\theta + \frac{1}{4} sin3\theta \right) \tag{4.6}$$

$$V_b = 1.15 V_{dq} \left(sin(\theta - \frac{2\pi}{3}) + \frac{1}{4} sin3\theta \right) \tag{4.7}$$

$$V_c = 1.15 V_{dq} \left(sin(\theta + \frac{2\pi}{3}) + \frac{1}{4} sin3\theta \right) \tag{4.8}$$

The modulation waveforms of one phase from the simulation are shown in Figure 4.1 for 1/6 THIPWM and Figure 4.2 for 1/4 THIPWM. The simulation is done under torque reference = 40Nm and speed reference = 2000rpm.
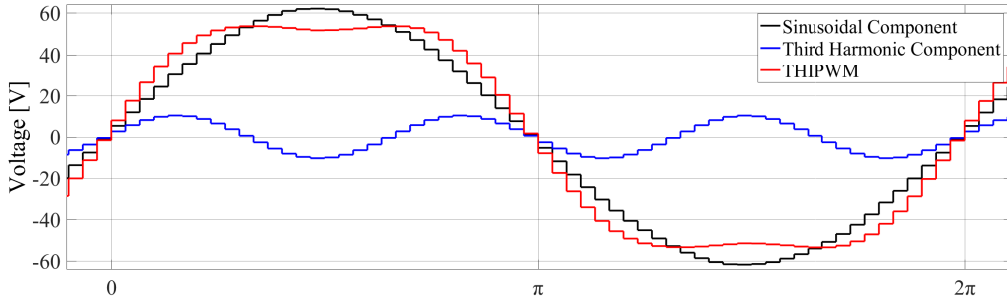
Figure 4.1: Reference voltage before and after 1/6 third harmonic injection
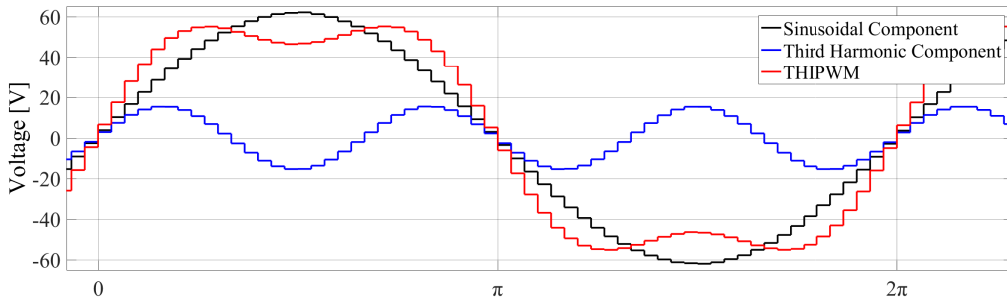
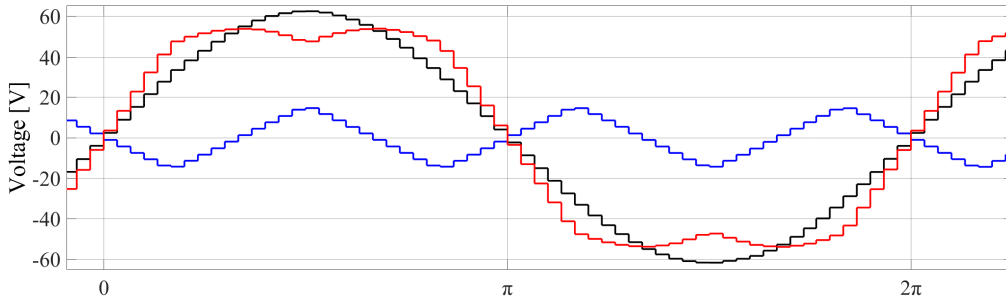**Figure 4.2:** Reference voltage before and after 1/4 third harmonic injection

4.2 SVM

There are two ways to realize SVM in a Simulink model, as is mentioned in Chapter 3.1.2., as division of zero vector SV_0 and SV_7 is equivalent to the injection of a specific common-mode component, and as a result, they produce the exact same results.

The easier way is to simply add the following third harmonic component to the three phase reference voltages.

$$U_{CM} = \frac{max(V_a, V_b, V_c) + min(V_a, V_b, V_c)}{2} \tag{4.9}$$

The modulation waveforms of one phase from the simulation are shown in Figure 4.3.

Figure 4.3: Reference voltage before and after triangular third harmonic injection

The more general way is to calculate the conducting time of different switching combinations. First, determine sector (from 1 to 6) from the rotating phasors' angle position using look-up table based on reference voltage signals in the $\alpha\beta$ coordinate. See figure 4.4 for the signal after sector determination. Next, convert the phasors in all six sectors to the first sector so that only SV_0, SV_7, SV_1 and SV_2 will form the target space vector.
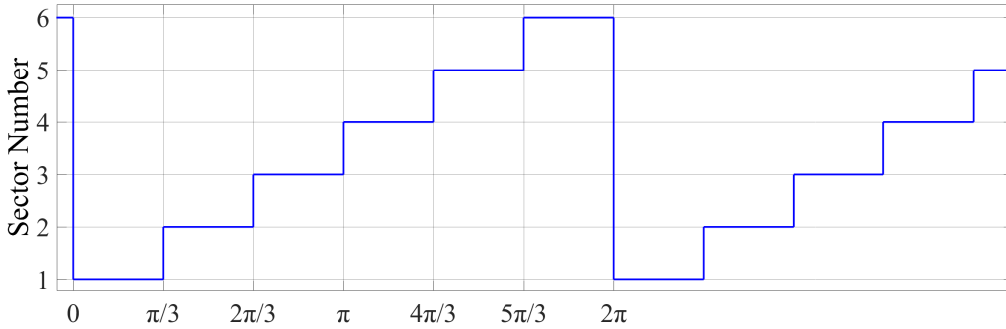
Figure 4.4: Sector determination

Then, the active time for SV_1 and SV_2 will be calculated. Consider an arbitrary target vector $\overline{V_0^*}$ in the first sector. The geometric summation can be mathematically expresses as

$$\overline{V_0^*} = V_0 \angle \theta_0 = \frac{T_{SV_1}}{\Delta T/2}\overline{SV_1} + \frac{T_{SV_2}}{\Delta T/2}\overline{SV_2} \tag{4.10}$$

for each switching period $\Delta T/2$, where T_{SV_1} and T_{SV_2} are the time for which space vector SV_1 and SV_2 are selected. Then, (4.10) can be further expressed as

$$\frac{\Delta T}{2}V_0 \angle \theta_0 = T_{SV_1} V_m \angle 0 + T_{SV_2} V_m \angle \frac{\pi}{3} \tag{4.11}$$

where $V_m = \frac{2}{3}V_{dc}$, which is the magnitude of the six active vectors.
Converting (4.11) into Cartesian form gives

$$\frac{\Delta T}{2}V_0(cos\theta_0 + jsin\theta_0) = T_{SV_1} V_m + T_{SV_2} V_m \left(cos\frac{\pi}{3} + jsin\frac{\pi}{3} \right) \tag{4.12}$$

31

Separating the real and imaginary components from the equation above gives

$$\frac{T_a}{2} = T_{SV_1} = \frac{V_0 sin\left(\frac{\pi}{3} - \theta_0\right)}{V_m sin\frac{\pi}{3}} \frac{\Delta T}{2} \tag{4.13}$$

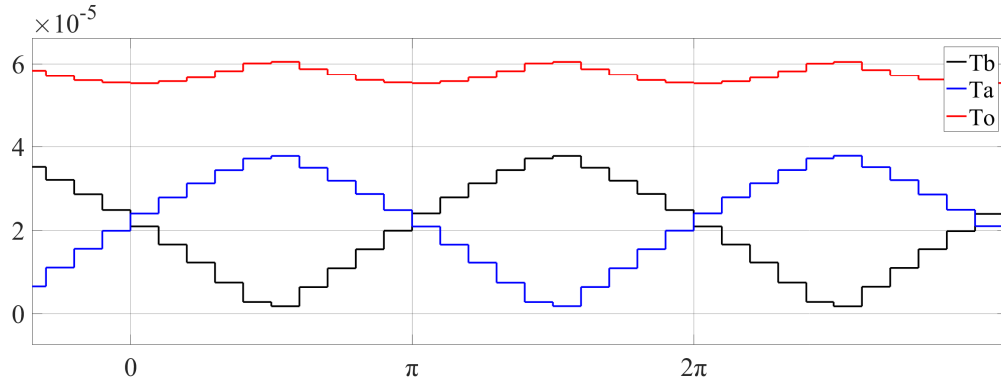$$\frac{T_b}{2} = T_{SV_2} = \frac{V_0 sin\theta_0}{V_m sin\frac{\pi}{3}} \frac{\Delta T}{2} \tag{4.14}$$

where m_a is the modulation index and $m_a = V_0/\left(V_m sin\frac{\pi}{3}\right) = V_0/\left(V_{dc}/\sqrt{3}\right)$.

The rest of the cycle $T_0 = \Delta T - T_a - T_b$ will be equally divided by SV_0 and SV_7. The following Fig. 4.5 illustrates the time relation again.
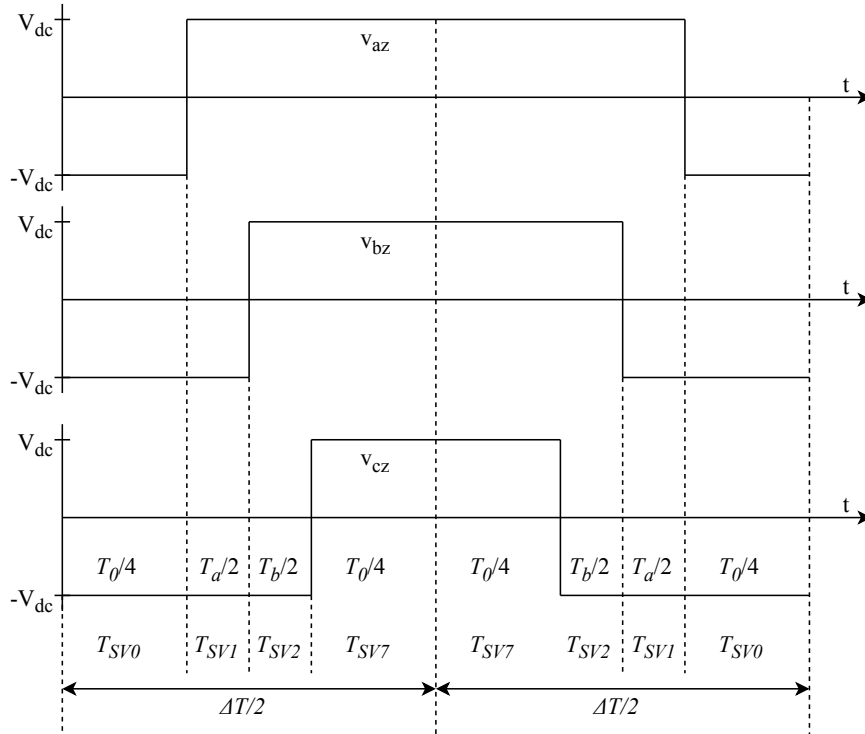
Figure 4.5: Time illustration

Waveform of T_a, T_b and T_0 are shown in Fig. 4.6.

Figure 4.6: T_a, T_b, T_0

Finally, based on which sector the rotating vector is located in, different combinations of T_a, T_b and T_0 are applied to three phase legs, according to Fig. 3.8. The modulation waveform of SVM is shown in Fig. 4.7.
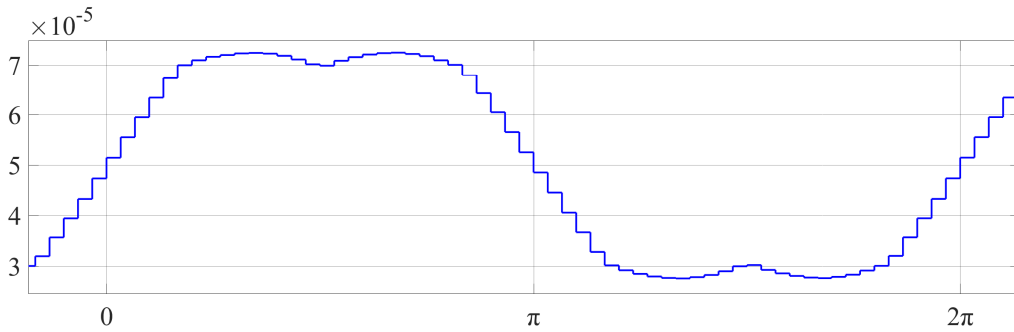
Figure 4.7: SVM modulation waveform

4.3 DPWM

Unified voltage modulation technique [17] [13] is applied to generate discontinuous PWM modulation waveforms. As is shown in Fig. 4.8, effective time T_{eff} denotes the time duration that different voltage is maintained and T_{eff} is also given by $T_{max} - T_{min}$, where $T_{max} = max(T_{as}, T_{bs}, T_{cs})$, $T_{min} = min(T_{as}, T_{bs}, T_{cs})$. When the gate signals for transistors are generated in the PWM algorithm, there is one degree of freedom where the effective time can be located anywhere arbitrarily within the half period. Therefore, a time-shifting parameter will be applied to generate the actual gate times (T_{ga}, T_{gb}, T_{gc}) for each leg, where the following relations are met.

$$T_{ga} = T_{as} + T_{offset} \tag{4.15}$$

$$T_{gb} = T_{bs} + T_{offset} \tag{4.16}$$

$$T_{gc} = T_{cs} + T_{offset} \tag{4.17}$$
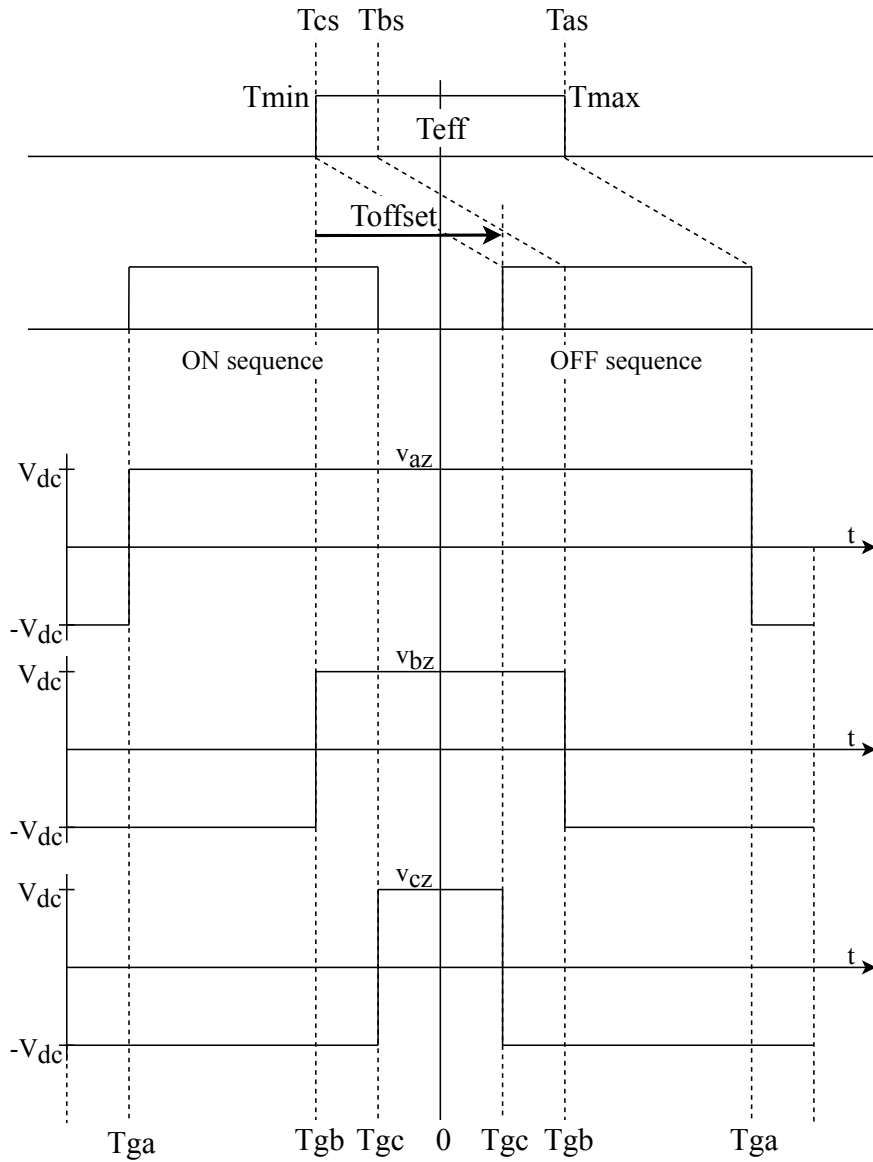
Figure 4.8: Unified voltage modulation

Restrictions should be applied as

$$T_{min} + T_{offset} \geq 0 \tag{4.18}$$

$$T_{max} + T_{offset} \leq T_s \tag{4.19}$$

Equation (4.18) and (4.19) give

$$-T_{min} = T_{offset.min} \leq T_{offset} \leq T_{offset.max} = T_s - T_{max} \tag{4.20}$$

Then, various DPWM schemes can be obtained by changing T_{offset} arbitrarily between $T_{offset.min}$ and $T_{offset.max}$.

For 60° DPWM, if the phase a voltage reference is positive/negative and has the maximum magnitude, the phase a switch should be clamped to the ON/OFF state. That is,

if

$$T_{min} + T_{max} \geq 0 \Rightarrow T_{max} + T_{offset} = T_s \Rightarrow T_{offset} = T_s - T_{max} \tag{4.21}$$

if

$$T_{min} + T_{max} < 0 \Rightarrow T_{min} + T_{offset} = 0 \Rightarrow T_{offset} = -T_{min} \tag{4.22}$$

For the +/- 30° shift cases, some modifications containing conditional sentences can be done accordingly.

For 60° DPWM, the switching pattern is opposite to that of the 60° DPWM. Therefore, the offset time is given by:
if

$$T_{min} + T_{max} \geq 0 \Rightarrow T_{max} + T_{offset} = T_s \Rightarrow T_{offset} = -T_{min} \tag{4.23}$$

if

$$T_{min} + T_{max} < 0 \Rightarrow T_{min} + T_{offset} = 0 \Rightarrow T_{offset} = T_s - T_{max} \tag{4.24}$$

For 120° DPWM, if +DC clamping

$$T_{offset} = T_s - T_{max} \tag{4.25}$$

if -DC clamping

$$T_{offset} = -T_{min} \tag{4.26}$$

All the equations above are implemented into the algorithm in Matlab script. Next, the reference voltage waveforms of one phase before and after modulation are shown as below, from Fig. 4.9 to Fig. 4.14. The equivalent common-mode components are also included in the figures. The simulations are done under the following conditions: torque reference = 40Nm, speed reference = 3000rpm.
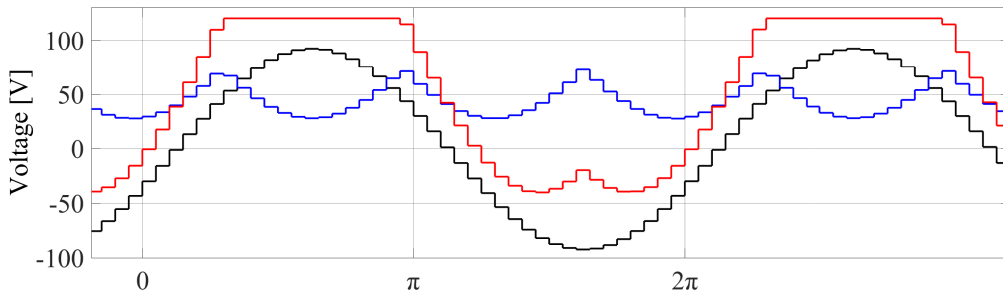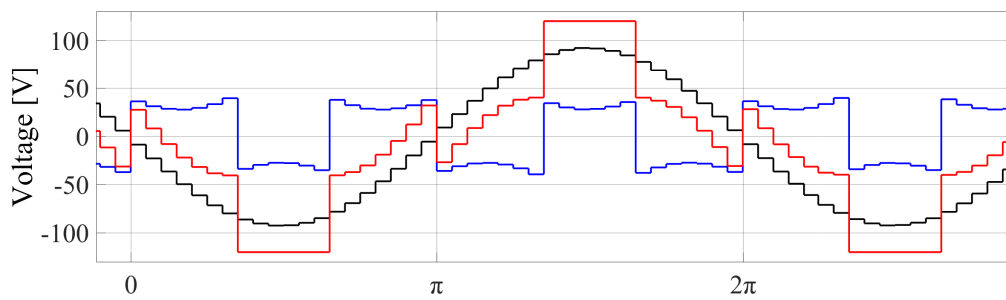

Figure 4.9: DPWMMAX
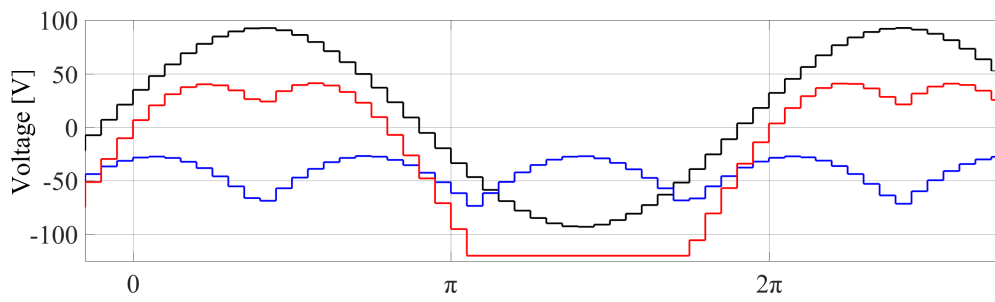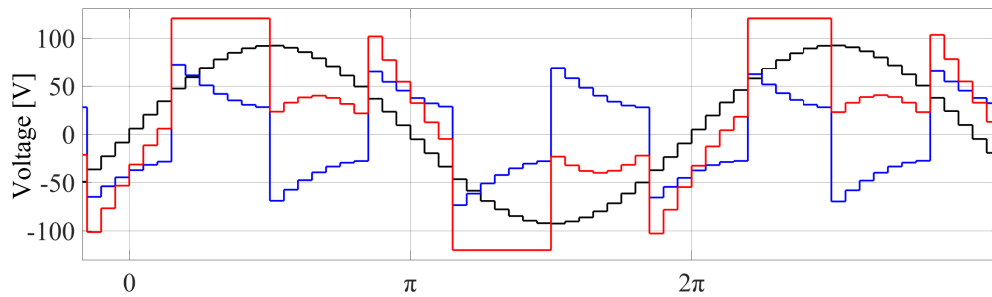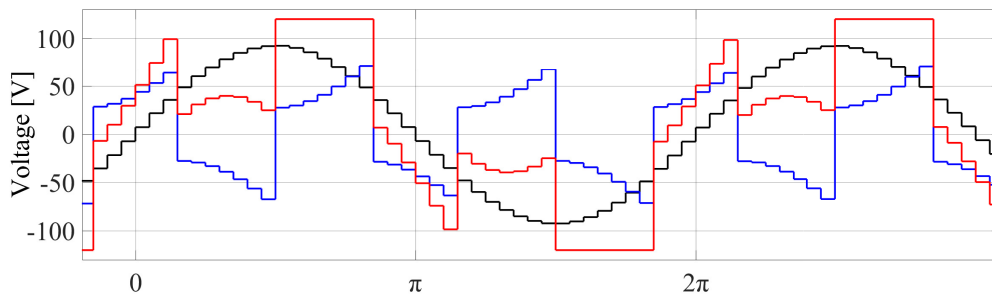
Figure 4.10: DPWMMIN

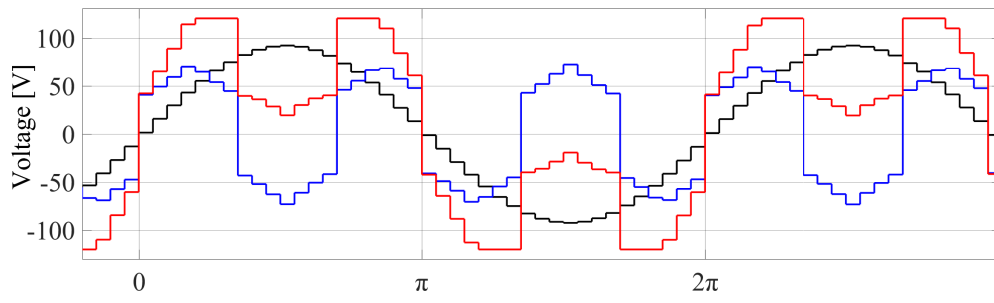**Figure 4.11:** DPWM1

Figure 4.12: DPWM0

Figure 4.13: DPWM2

Figure 4.14: DPWM3

5

Results and analysis

In this chapter, important parameters including current THD, inverter conduction losses, switching losses and efficiency, are going to be measured and calculated. They will be demonstrated in the form of speed-torque maps intuitively. The map differences will be presented and analyzed in order to find out the most suitable modulation method in different areas of the motor operating map under different requirements. Driving cycle tests are made to measure the inverter energy losses in a more practical way. Comparison based on switching frequency variation is also made in the form of line plots.

5.1   Phase current THD comparison

Taking SVM for example, as is shown in the THD map of SVM in Fig. 5.1, a typical current THD map has the following characteristics: In the low torque region where the phase current magnitude is relatively low, THD is high; In the high torque region, on the contrary, THD is low. However, the THD contour is not necessarily horizontal. As is seen in Fig. 5.2 and Fig. 5.3, under the same torque level, the harmonic spectrum of the phase current still shows different behaviors.
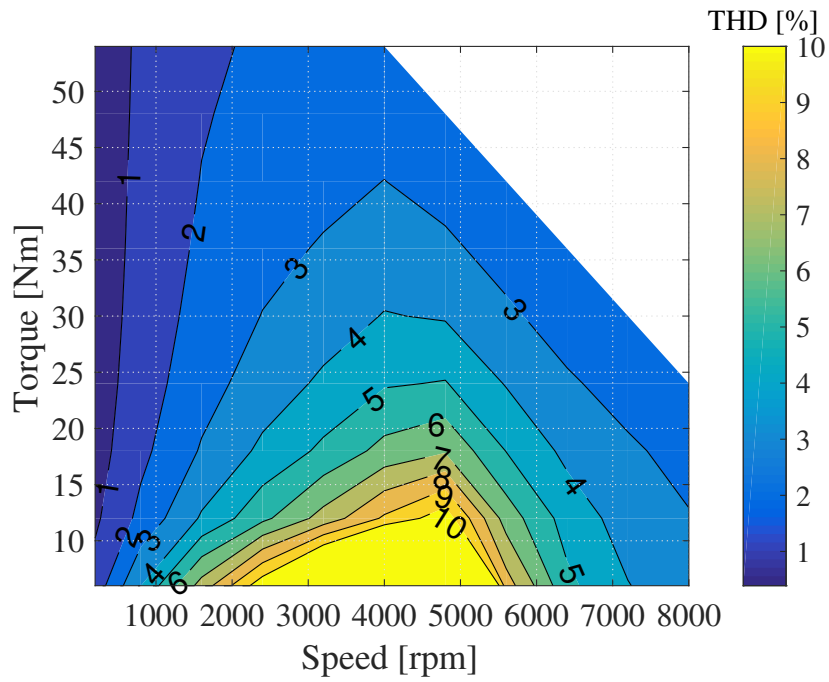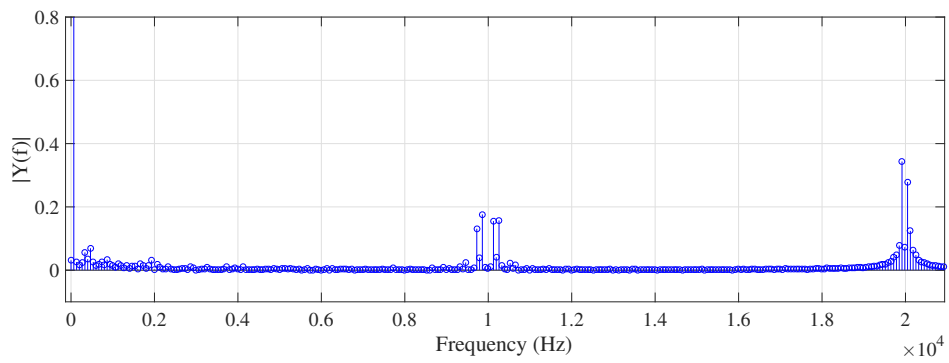
Figure 5.1: THD map of SVM

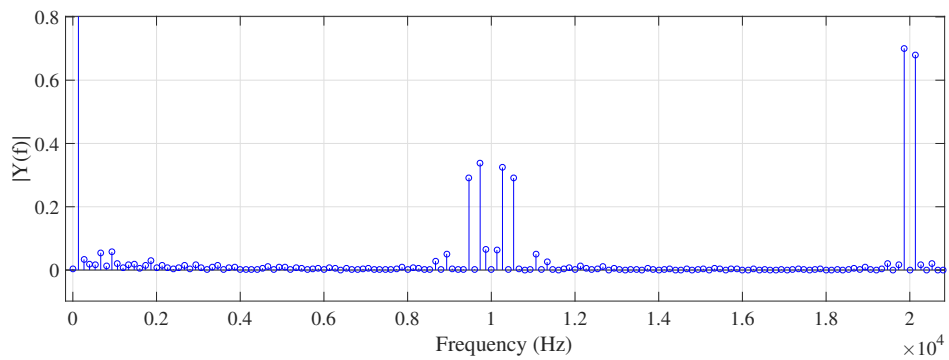**Figure 5.2:** Harmonic spectrum under 800 rpm, 12 Nm

Figure 5.3: Harmonic spectrum under 1600 rpm, 12 Nm

When the torque is zero in the non-field-weakening region, i_d and i_q will both be zero, and only harmonics exist, which result in infinite high current THD; in the field-weakening region, i_q will still be zero and THD is still very high. The area where torque is below 5 Nm is not plotted for a better scale of the map.

Another factor that affects the measure of THD is the Simulink solver setting. A sensitivity analysis on 'relative tolerance' is done at the operation point of 800 rpm and 12 Nm of SVM method. The default value of relative tolerance is 1e-3, which is a percentage of the state's value, i.e., a computed accuracy within 0.1 %. The THD results are shown in Fig. 5.4. This selection is a trade-off between the simulation accuracy and the cost of time. As increasing relative tolerance from 1e-5 to 1e-6 will not make a big difference on THD result but only slow down the simulation, the relative tolerance is finally set to 1e-5 and the maximum step size is set to 'auto'.
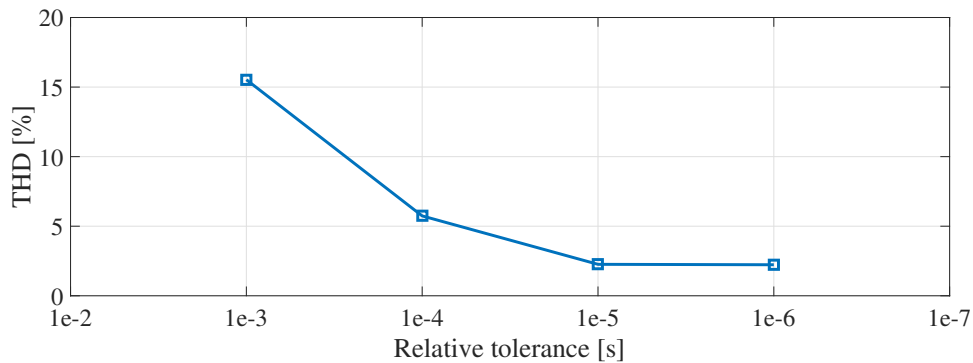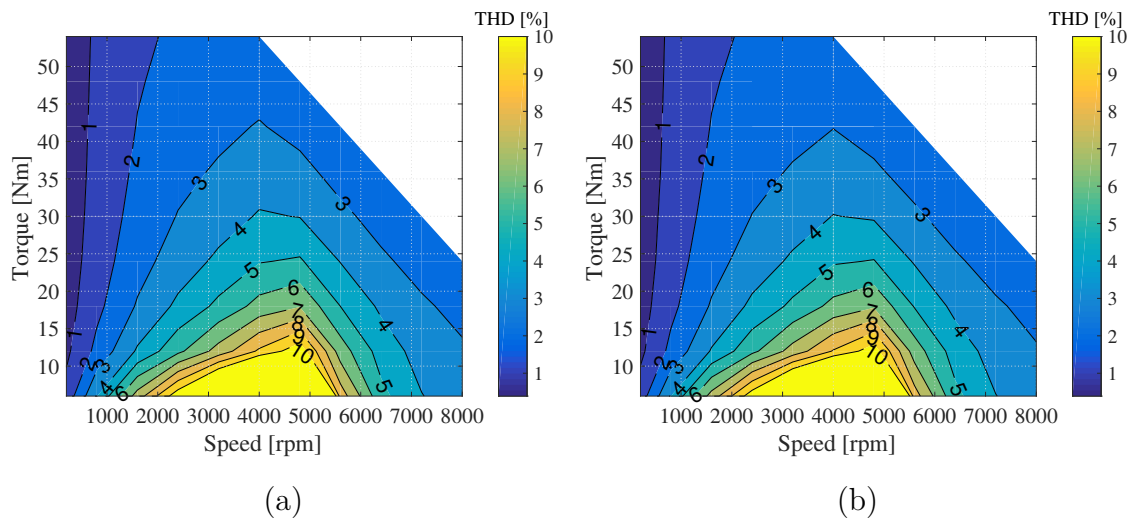

**Figure 5.4:** Relative tolerance's influence on THD

Now, a couple of THD map comparisons will be presented as follows.

The THD maps of 1/6 THIPWM and 1/4 THIPWM are shown in Fig. 5.5. In Fig. 5.6, a THD difference map is made based on them. It can be concluded that in most of the operating region, the current harmonics are higher for 1/6 THIPWM.
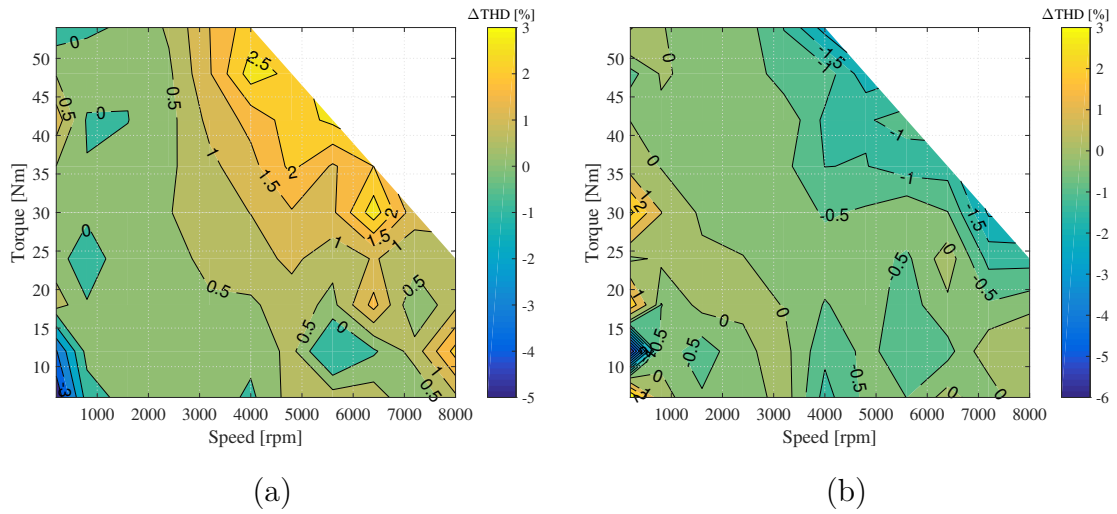
Figure 5.5: (a) THD map of 1/6 THIPWM (b) THD map of 1/4 THIPWM
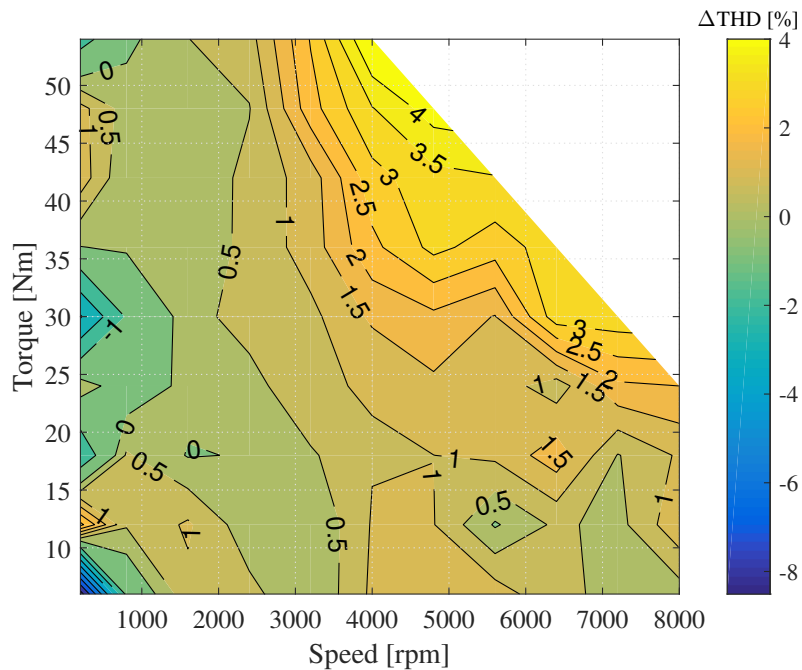
Figure 5.6: THD difference
$$\Delta THD = 100(THD_{1/6\,THIPWM} - THD_{1/4\,THIPWM})/THD_{1/4\,THIPWM}$$

The THD differences between SVM and two THIPWM methods are relatively small and the difference maps are shown in Fig. 5.7. From those plots, it can be concluded that for CPWM, THD increases in the following order: 1/4 THIPWM, SVM, 1/6 THIPWM.
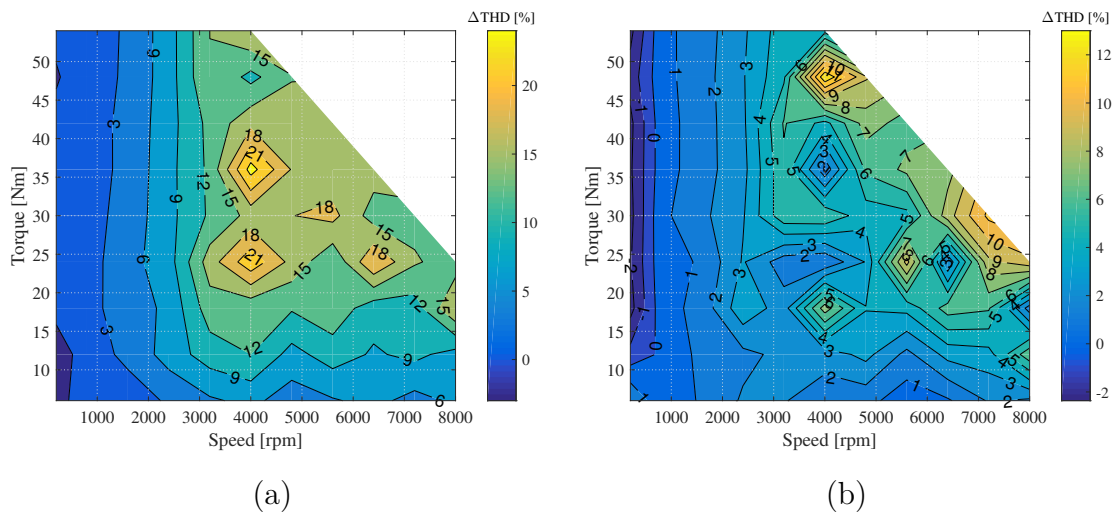
(a)   (b)

Figure 5.7: (a) THD difference
$\Delta THD = 100(THD_{1/6\,THIPWM} - THD_{SVM})/THD_{SVM}$ (b) THD difference
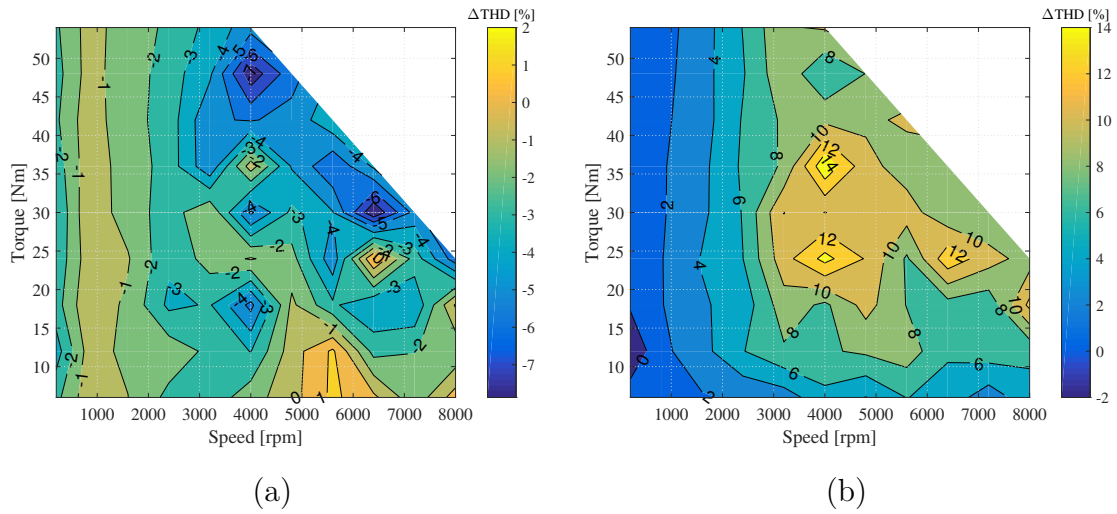$\Delta THD = 100(THD_{1/4\,THIPWM} - THD_{SVM})/THD_{SVM}$

For DPWM, it turns out that THD increases in the following order: DPWM2, DPWM3, DPWMMAX/DPWMMIN, DPWM1, DPWM0. The difference maps between the neighbouring pairs are shown as follows:

(a)   (b)

Figure 5.8: (a) THD difference
$\Delta THD = 100(THD_{DPWM3} - THD_{DPWM2})/THD_{DPWM2}$ (b) THD difference
$\Delta THD = 100(THD_{DPWMMAX} - THD_{DPWM3})/THD_{DPWM3}$

(a)   (b)

Figure 5.9: (a) THD difference
$\Delta THD = 100(THD_{DPWMMAX} - THD_{DPWM1})/THD_{DPWM1}$ (b) THD difference
$\Delta THD = 100(THD_{DPWM0} - THD_{DPWM1})/THD_{DPWM1}$

Generally, under the same frequency, CPWM has a better harmonic performance than DPWM, where the difference is shown in Fig. 5.10, taking SVM and DP-WMMAX for example. However, it should be noticed that DPWM provides the possibility to further increase the switching frequency since fewer switching takes place. Therefore, there is room for DPWM to improve THD performance given a higher switching frequency, at the expense of increased switching losses. The THD variation with the switching frequency will be investigated in Chapter 5.4.
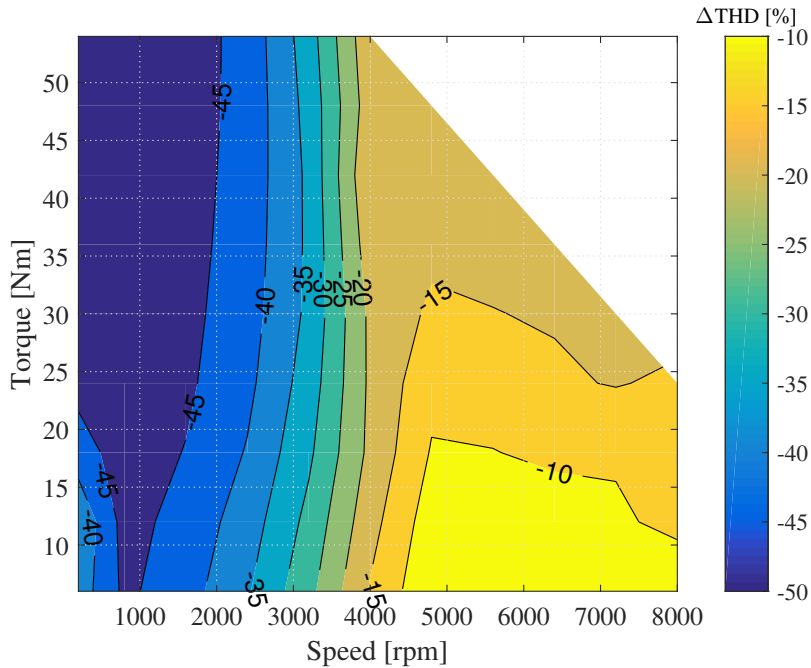
Figure 5.10: THD difference
$\Delta THD = 100(THD_{SVM} - THD_{DPWMMAX})/THD_{DPWMMAX}$

However, in this system, the simulation results show that DPWM2, the one with the lowest THD among all DPWM methods, can even perform better than 1/4 THIPWM in the high speed region of the map. While in the low speed region, 1/4 THIPWM still has lower THD than DPWM2. The THD map of DPWM2 is shown in Fig. 5.11 and difference map is shown in Fig. 5.12.
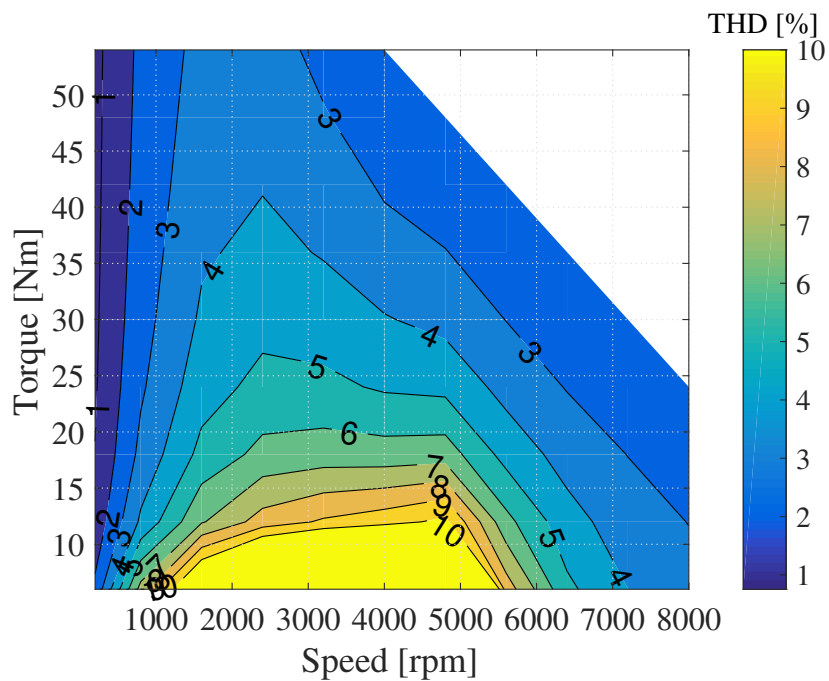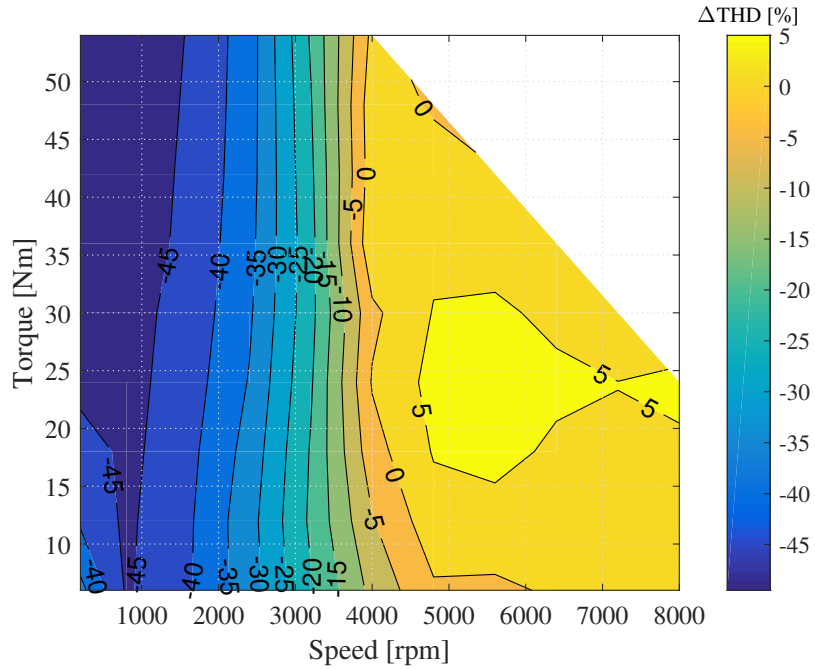

Figure 5.11: THD map of DPWM2

Figure 5.12: THD difference
$$\Delta THD = 100(THD_{1/4\,THIPWM} - THD_{DPWM2})/THD_{DPWM2}$$

From all the plots above, it can be concluded that in general, continuous PWM methods has lower current harmonics than discontinuous PWM methods. However, in order to achieve the lowest THD in the machine operating map, DPWM2 is to be selected in the area where the speed is over approximately 4000 rpm and 1/4 THIPWM is optimal for the operating points where the speed is below approximately 4000 rpm.

5.2 Inverter losses and efficiency comparison

In this section, according to the formula in the theory chapter, the conduction loss, the switching loss, the total loss as well as the inverter efficiency will be calculated and plotted in the maps. Detailed comparisons will be made to figure out the favorable choices of modulation methods.
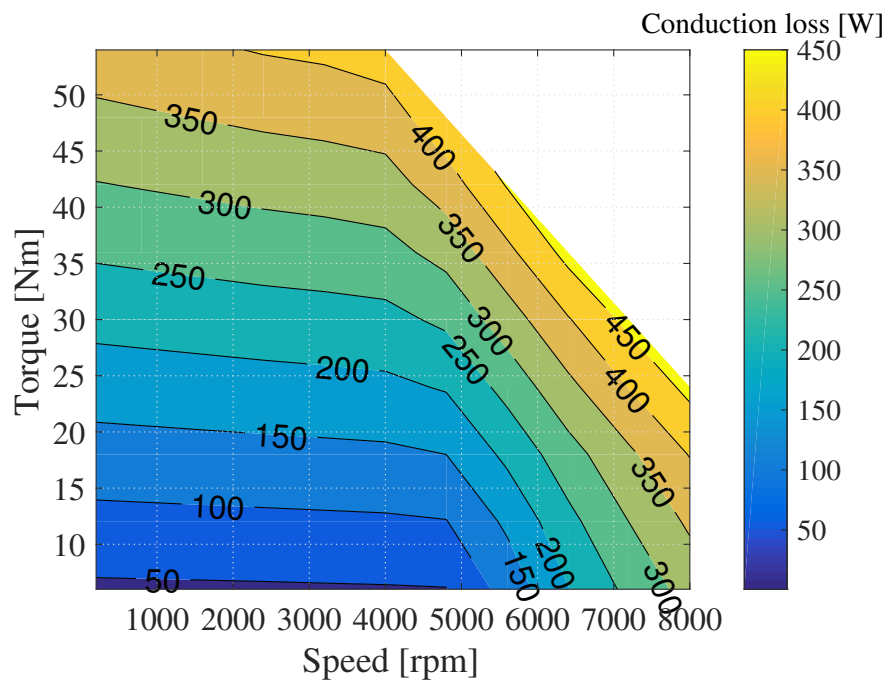
5.2.1 Conduction losses

As the differences among each modulation method are barely noticeable, the conduction losses map of SVM in Fig. 5.14 will be explained briefly. The inverter's conduction loss is summed up with six transistors' conduction losses. As the conduction loss is proportional to the phase current amplitude and this amplitude is plotted in Fig. 5.13, therefore, it will have a similar shape as the current amplitude but is also influenced by the phase angle, which will be illustrated later. When the torque is higher, the phase current is larger and it leads to higher conduction

losses. In the field weakening region, higher d-axis current also contributes to higher conduction losses.
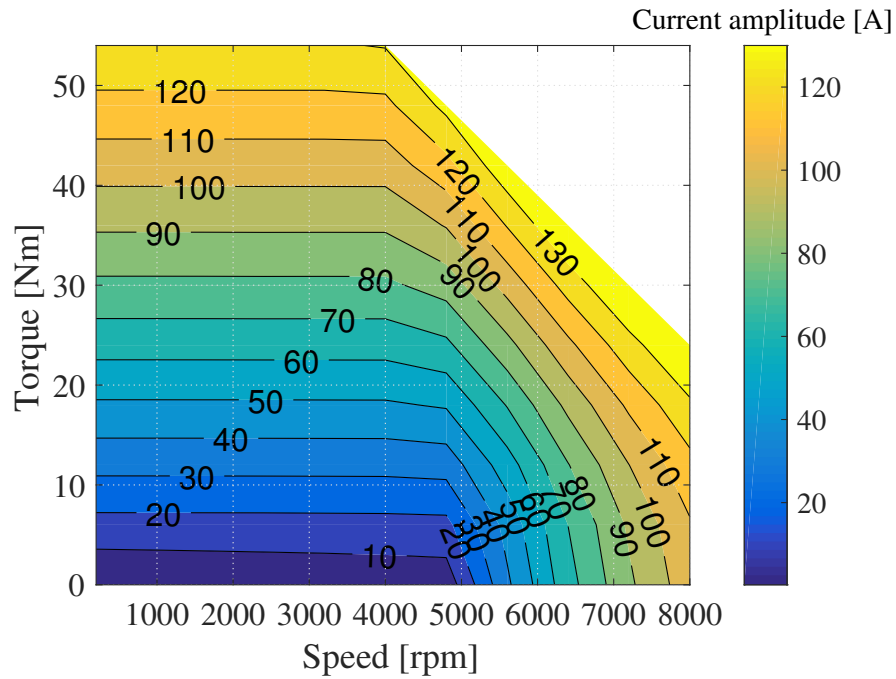
**Figure 5.13:** Phase current amplitude for SVM

**Figure 5.14:** Conduction loss map for SVM

5.2.2   Switching losses

For all three CPWM methods, the switching loss maps looks the same. The switching loss is proportional to peak phase current amplitude as well, similar to the conduction loss calculation as is analyzed in the previous chapter.

However, from the comparison between CPWM and DPWM, taking SVM and DPWM3 for example in Fig. 5.15 and Fig. 5.16, it is clear that DPWM cuts switching losses almost by half roughly.
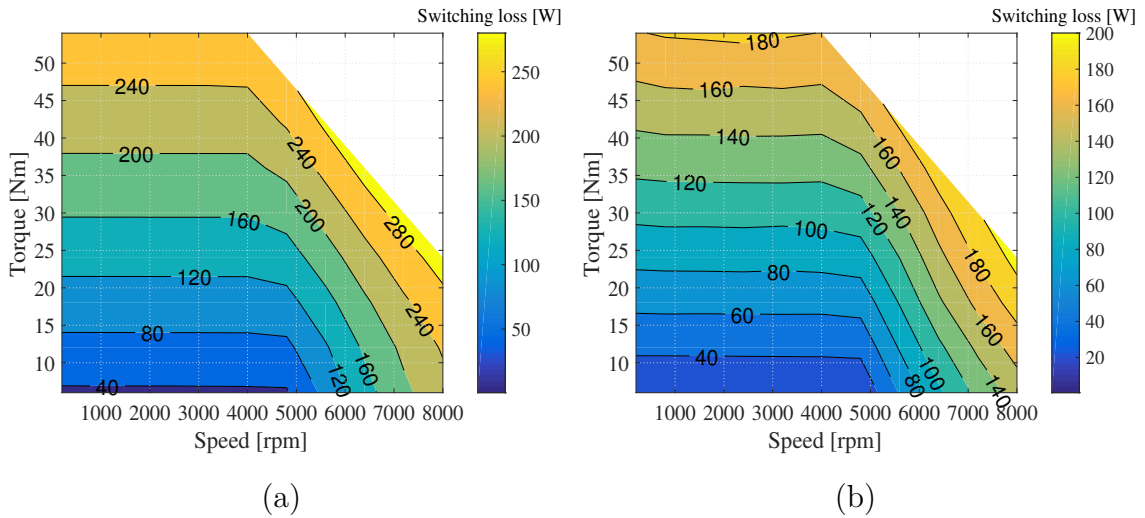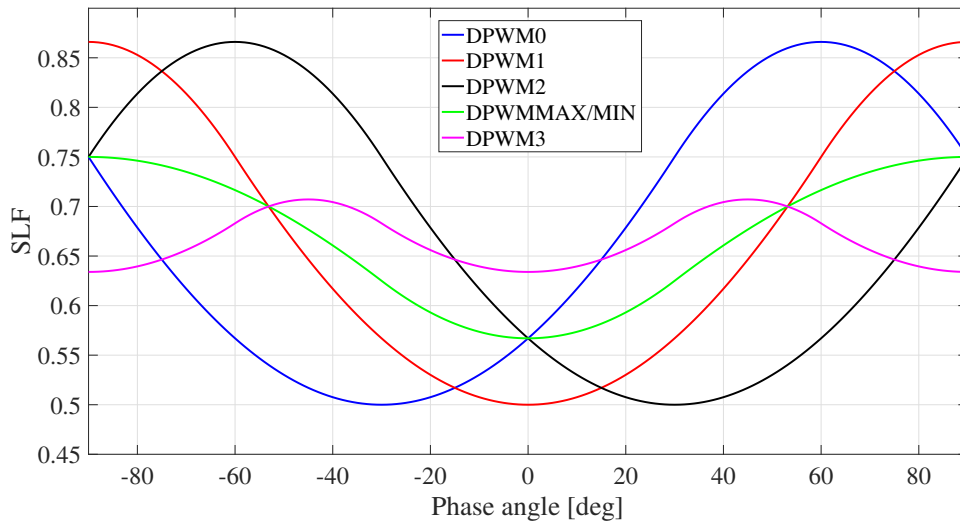

Figure 5.15: (a) Switching loss map of SVM (b) Switching loss map of DPWM3
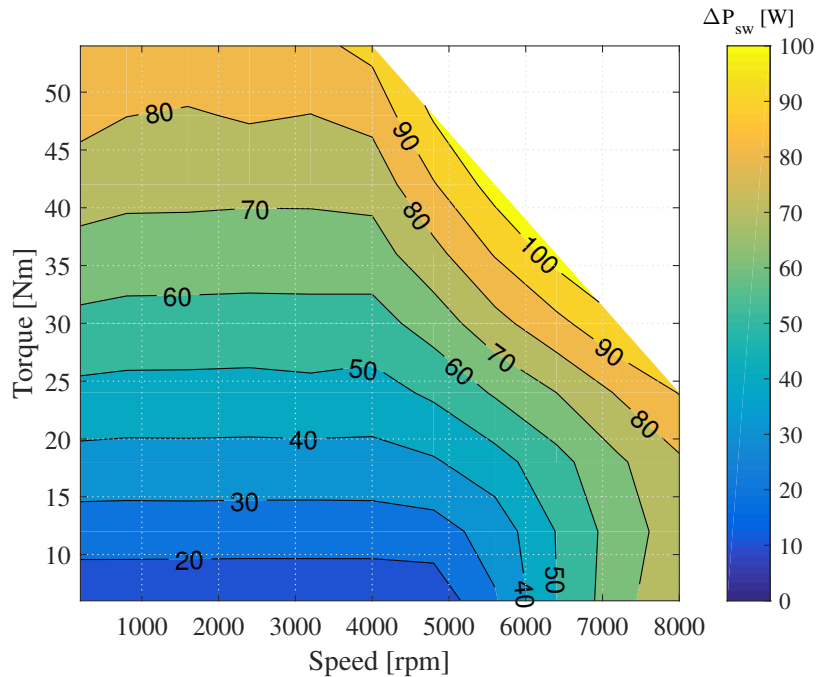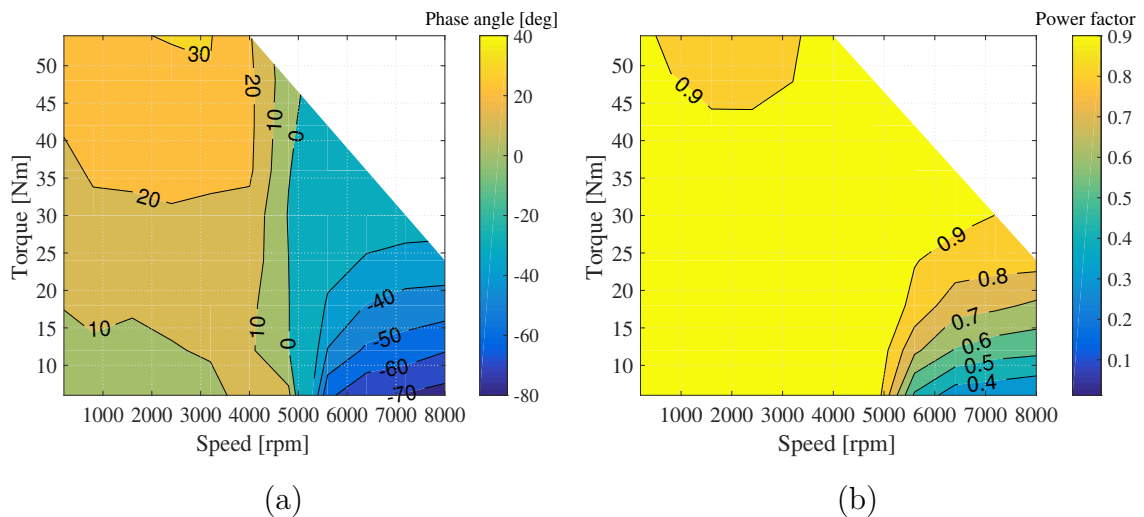

Figure 5.16: Switching loss difference $\Delta P_{sw} = P_{sw_{SVM}} - P_{sw_{DPWM3}}$

For different DPWM methods, from all the SLF functions presented in Chapter 3.2.3.2, the characteristics can be graphically shown in Fig. 5.17. The phase angle and power factor distributions are demonstrated in Fig. 5.18 below.
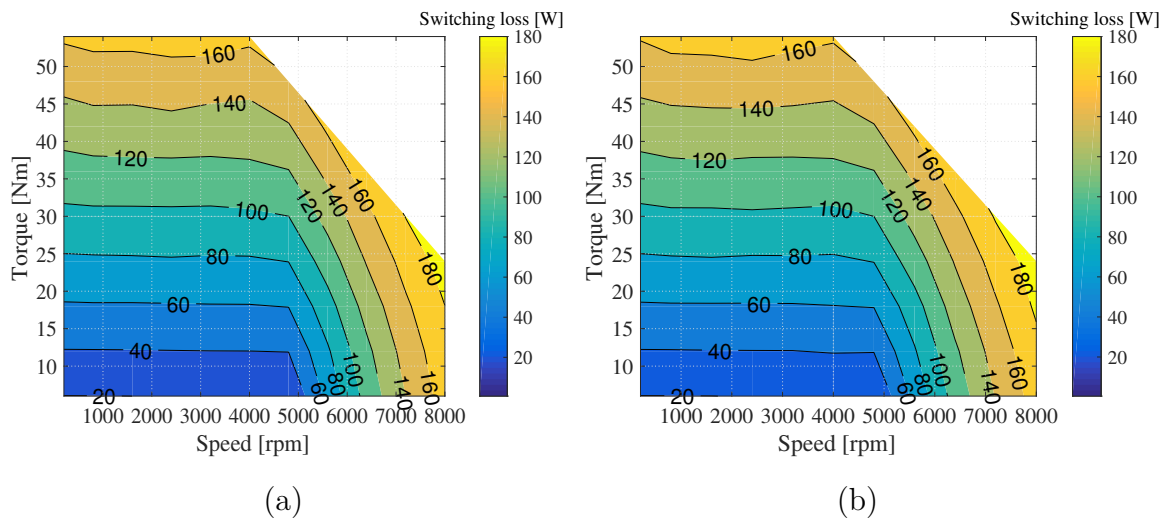

Figure 5.17: SLF characteristics of DPWM methods under $SLF_{CPWM} = 1$
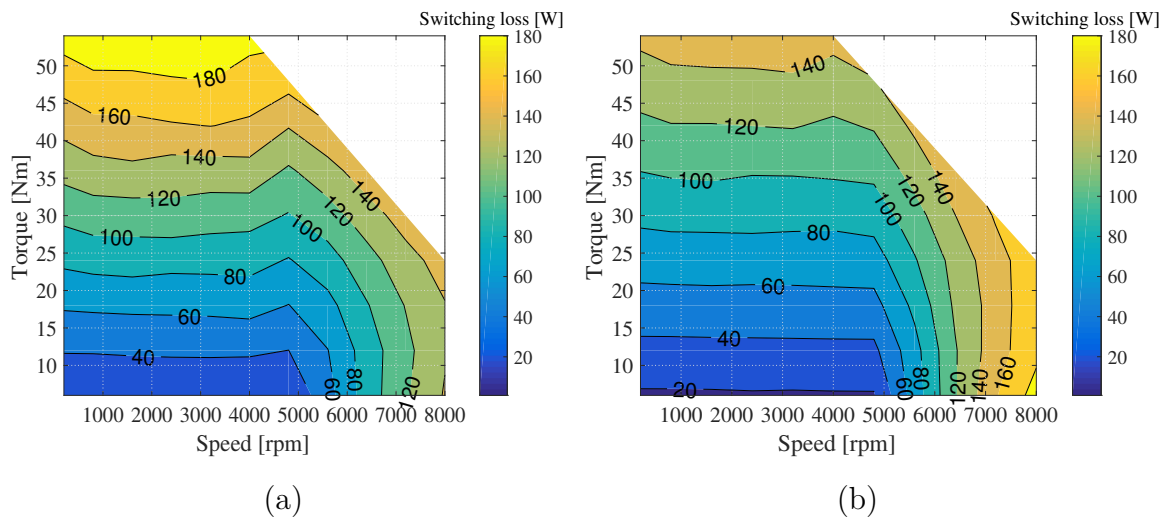

Figure 5.18: (a) Phase angle map (b) Power factor map

Then, switching loss maps of all DPWM methods are presented below. No difference map is plotted since the switching loss distribution map is already very identical for each method.
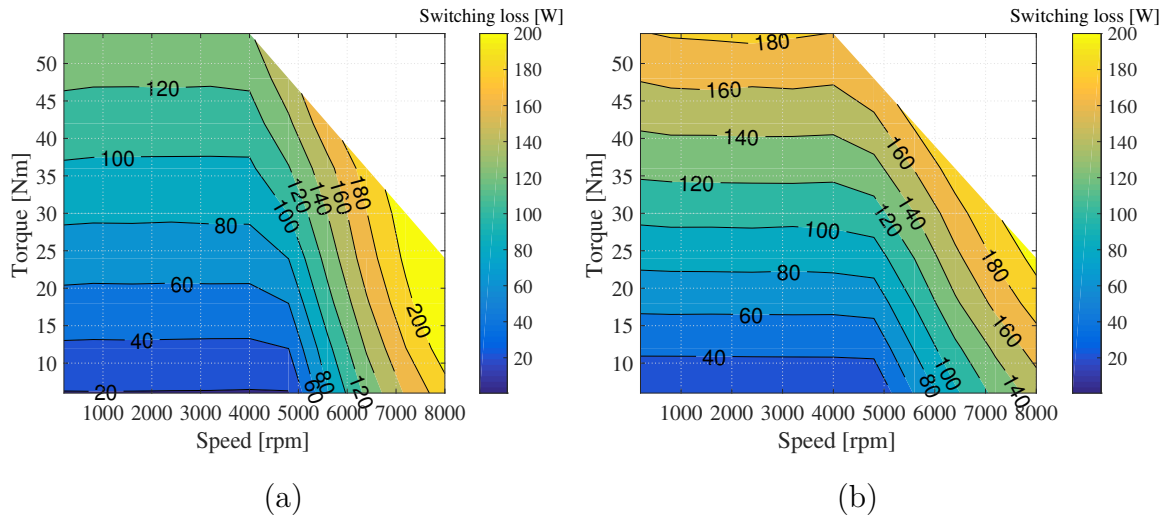
Figure 5.19: (a) P_{sw} map of DPWMMAX (b) P_{sw} map of DPWMMIN

Figure 5.20: (a) P_{sw} map of DPWM0 (b) P_{sw} map of DPWM1

Figure 5.21: (a) P_{sw} map of DPWM2 (b) P_{sw} map of DPWM3

It can be concluded from above that, since phase angle differs a lot in different regions of the operating map, there is a combination of DPWM methods that makes up the optimal solution of the lowest switching losses, rather than one favorable DPWM method. Thus, in order to reach the lowest switching losses, the modulation technique should be selected according the following table.

Table 5.1: DPWM METHOD SELECTION BASED ON SWITCHING LOSSES

Phase Angle [deg]	Best DPWM Method with the lowest Psw	Corresponding Region in the Map
[-90, -75]	DPWM3	Non-existing
[-75, -15]	DPWM0	Most of the field-weakening region
[-15, 15]	DPWM1	Area near the base speed
[15, 75]	DPWM2	Most of the non-field-weakening region
[75, 90]	DPWM3	Non-existing

5.2.3 Total losses

Making a comparison between CPWM and DPWM is sufficient to illustrate the difference. The result is shown in Fig. 5.22 and Fig. 5.23 using SVM and DPWM3 for example again. Obviously, CPWM has a higher inverter total loss compared to DPWM. Regarding the differences among those DPWM methods, it is basically the same conclusion as is shown in the previous chapter since the conduction losses for all methods are considered to be the same.
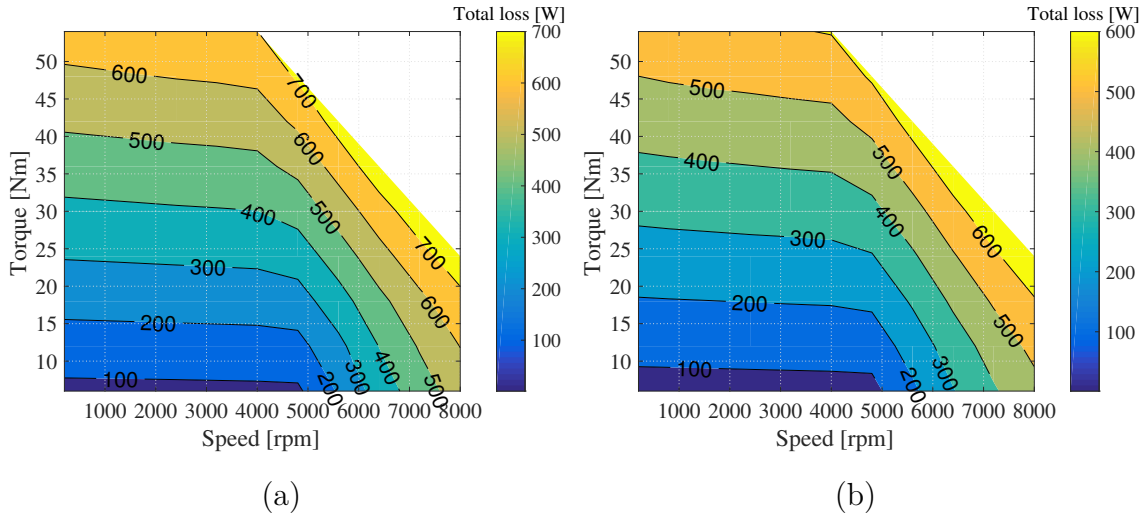
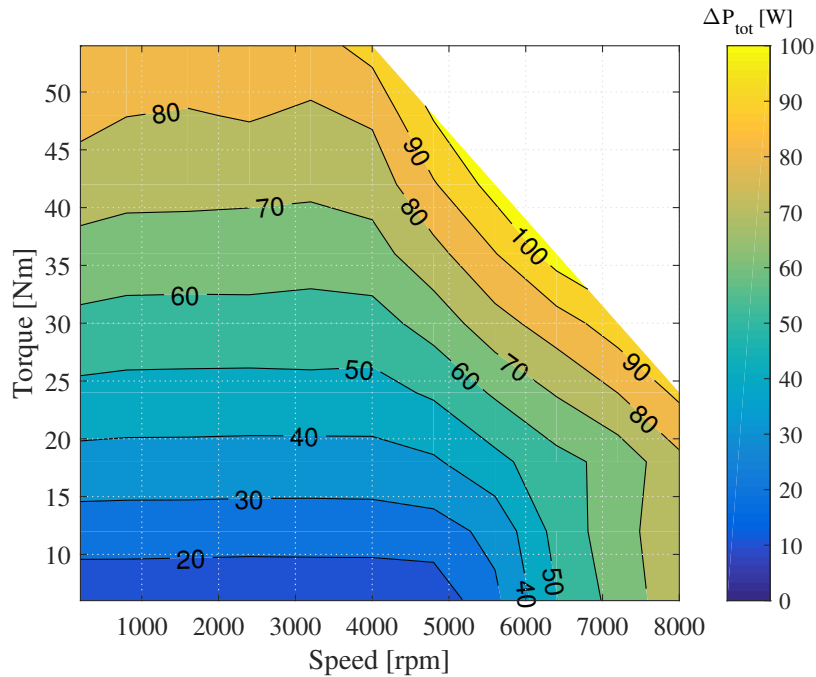**Figure 5.22:** (a) Total loss map of SVM (b) Total loss map of DPWM3

Figure 5.23: Total inverter loss difference $\Delta P_{tot} = P_{tot_{SVM}} - P_{tot_{DPWM3}}[W]$

5.2.4 Inverter efficiency

From Fig. 5.24 and Fig. 5.25, it is clear that continuous PWM methods such as SVM have lower inverter efficiency than discontinuous ones such as DPWM3. Also, it can be seen from the efficiency map that in the high speed low torque region, as field weakening creates a high speed, the output reactive power contributes to a large proportion of the total output power. As the losses of the inverter is related to the current magnitude which contains both active and reactive current, the efficiency in this region is reduced.
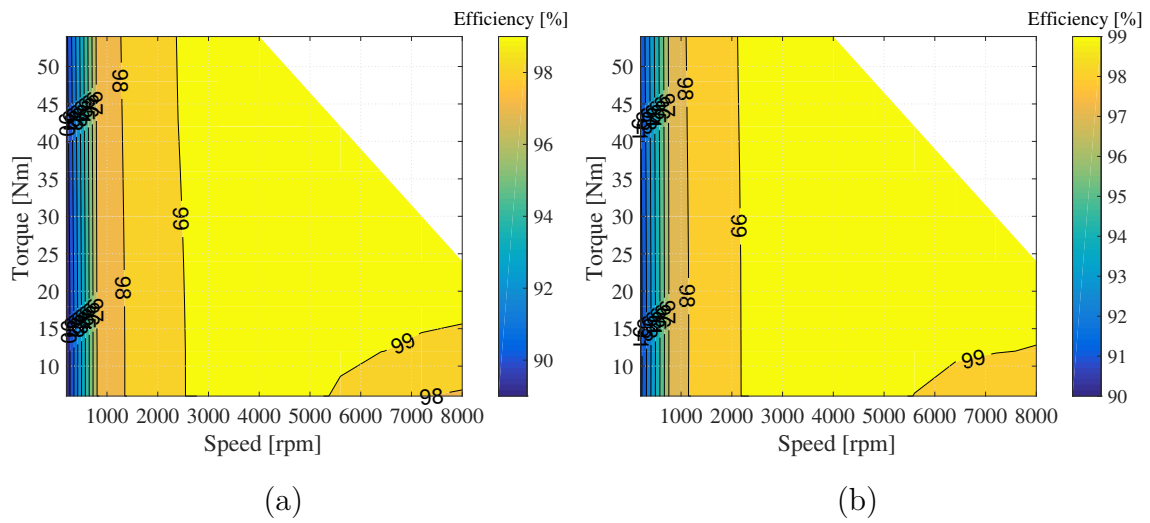
Figure 5.24: (a) Inverter efficiency map of SVM (b) Inverter efficiency map of DPWM3
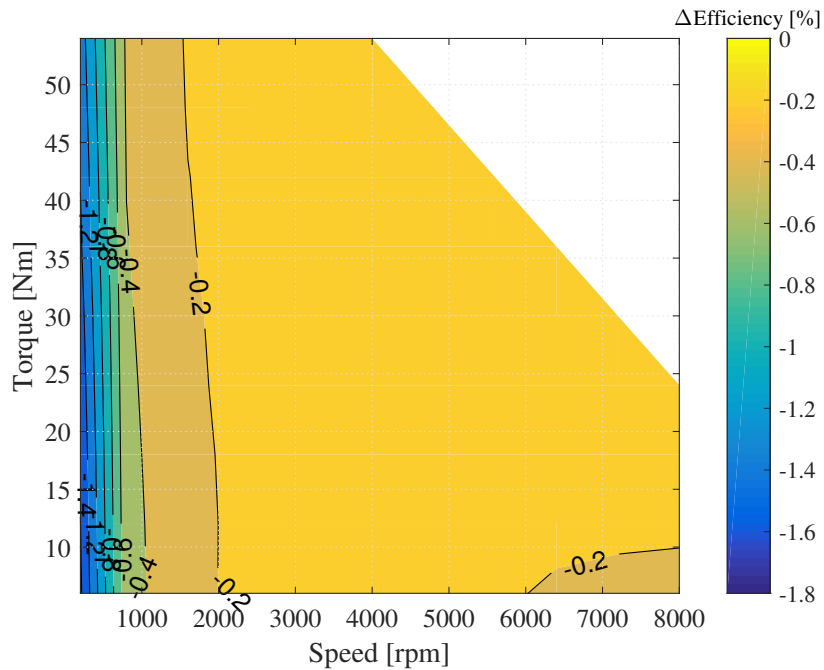

Figure 5.25: Inverter efficiency difference $\Delta \eta = \eta_{SVM} - \eta_{DPWM3}[\%]$

The efficiency comparison among DPWM methods is again highly dependent on the phase angle. For each method, if the switching loss is high, then the overall efficiency is low, and vise versa. The map plots are omitted here.

5.3   Comparison based on driving cycles

5.3.1   ECE

Based on the inverter total losses map plotted in Chapter 5.2.3, operating points of an ECE driving cycle are marked as red dots in the map, as is shown in Fig. 5.26, taking the result of SVM model for example first.
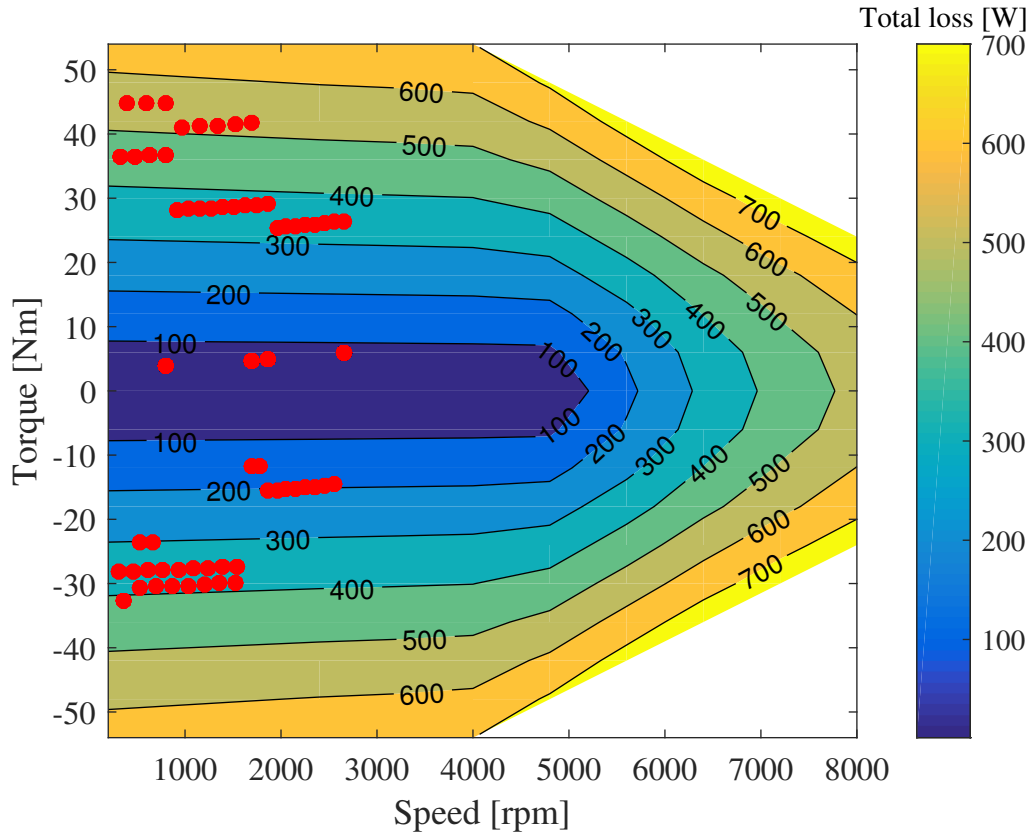
Figure 5.26: ECE operating points on SVM total loss map

Since the map is only made of 179 valid data points, the operating points located in the rest of the map area will not lead to a power loss result directly. Thus, the Neural Net (NNET) Fitting toolbox of Matlab is used to predict the unknown values. An artificial neural network is a network of simple elements called artificial neurons, which receive the input, change their internal state (activation) according to the input and produce the output depending on the input and activation. An artificial neuron mimics the mechanism of a biophysical neuron with inputs and outputs. The network is formed by connecting the output of certain neurons to the input of other neurons forming a directed and weighted graph. The weights as well as the functions that compute the activation can be modified by a process called learning, which is governed by a learning rule[18].

Two inputs (speed, torque) and one target (power loss) are manually inserted from workspace in the form of matrices. Bayesian Regularization algorithm is used for

training as this algorithm typically is suitable for difficult, small or noisy datasets. The dataset of 179 samples is very small. Next, 75 % of the samples are used for training, 5 % for validation and the rest 20 % for testing. Bayesian Regularization algorithm does not require validation process so the validation samples are set to a minimum. The samples are randomly divided into these three groups each time training or retraining starts. The samples for testing will have no effect on training and provide independent measurement of the network performance. Two-layer (i.e. one hidden layer + one output layer) feed forward neural network is selected as it can fit any input-output relationship given enough neurons in the hidden layer. Moreover, this problem is just 2-dimensional and looks quite linear. Before training starts, the last parameter to be determined is the number of hidden neurons. After training multiple times for different number of hidden neurons, performance plot, error histogram plot and regression plot are compared to find out the suitable value of hidden neurons. The performance plot tells the mean squared error of the training and testing, which is the lower, the better. The error histogram intuitively shows the error distribution where both the large error instances and the number of instances around zero error should be compared. The regression plot shows the regression R which measures the correlation between the output and the target. R should be as close to 1 as possible. When trying out different numbers of hidden neuron numbers, one optimal result for each case selected based on the requirements above will be kept for the final comparison after multiple retraining. When all the optimal results are gathered together, it is easy to conclude: When the number of hidden neurons is high, or even close to the total number of samples, overfitting happens, i.e., even the training set performs very well in the error histogram, the testing sample distribution is poor; When the number of hidden neurons is low, the whole network simply performs bad and the errors are not minor. The number of hidden neurons is finally determined to be 40. A series of results are presented in Fig. 5.27, Fig. 5.28 and Fig. 5.29. The testing set has a mean squared error of 10.03 which is relatively low. The error histogram of testing samples shows an acceptable result where the largest deviation is only 11.13. The number of the samples is so small that a curve fitting with even higher accuracy is hard to achieve. Regression R turns out to be very close to 1 as the output matches the target very well. Finally, the code of the neural network is generated and the input speed and torque can be anywhere in the map.
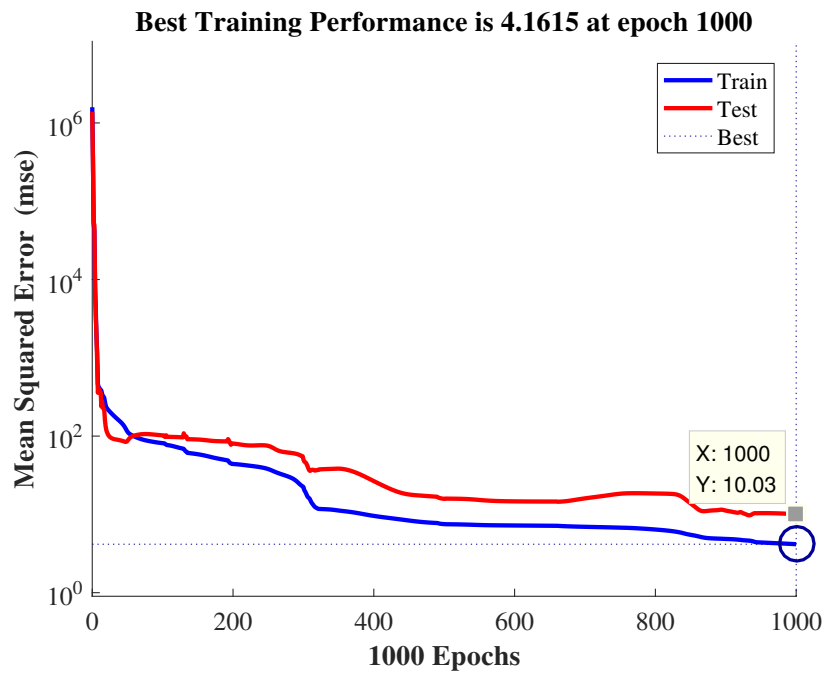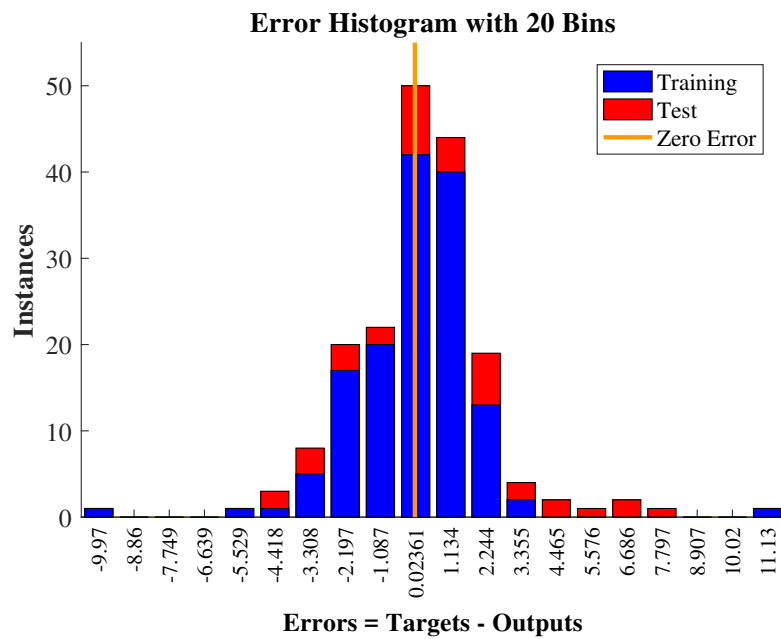
Figure 5.27: Performance
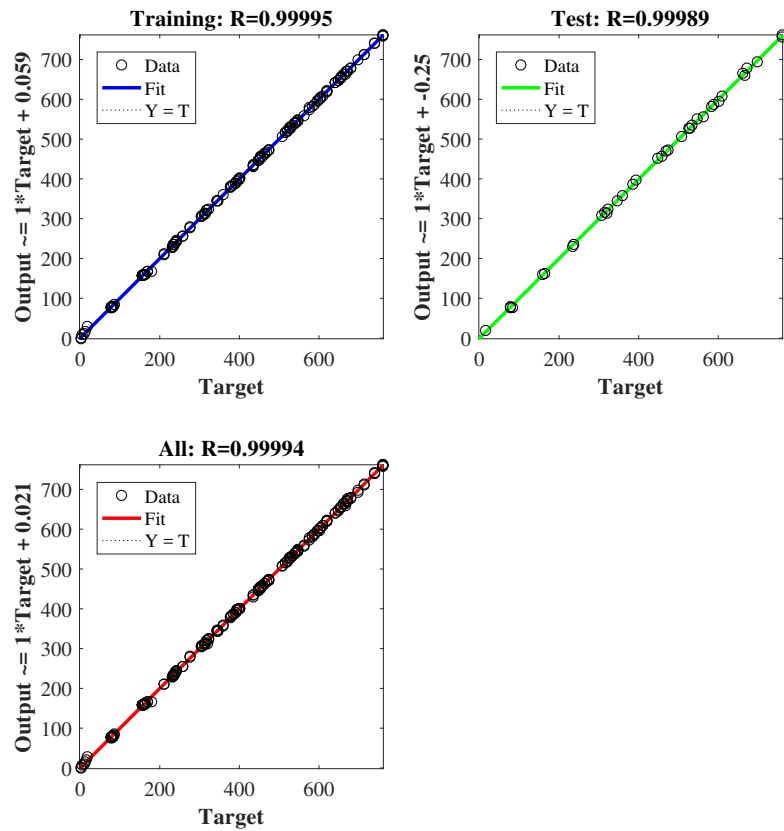

Figure 5.28: Error histogram

Figure 5.29: Regression

The inverter total loss versus time with a SVM model under ECE driving cycle is plotted in Fig. 5.30. After integrating the curve, the total energy loss W is calculated to be $0.0338[kWh]$.
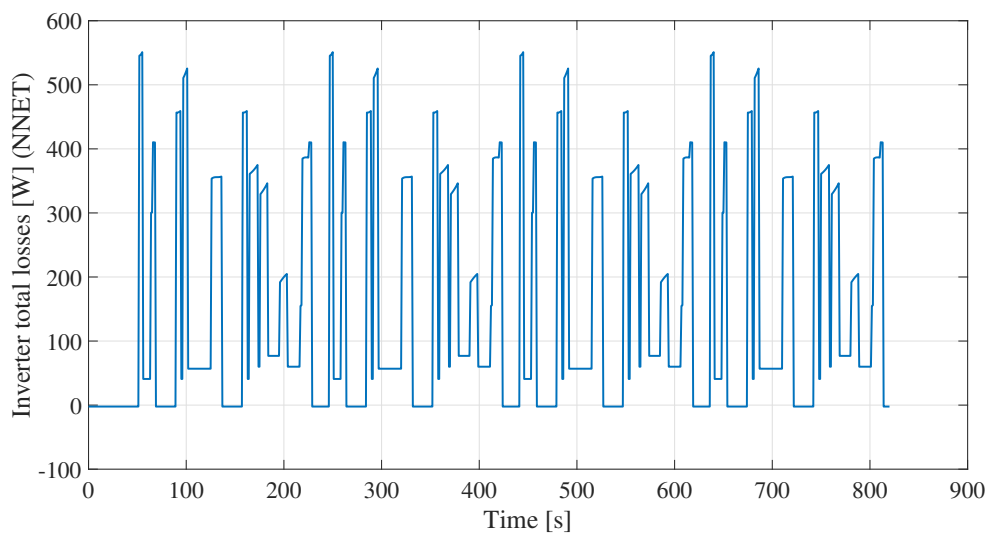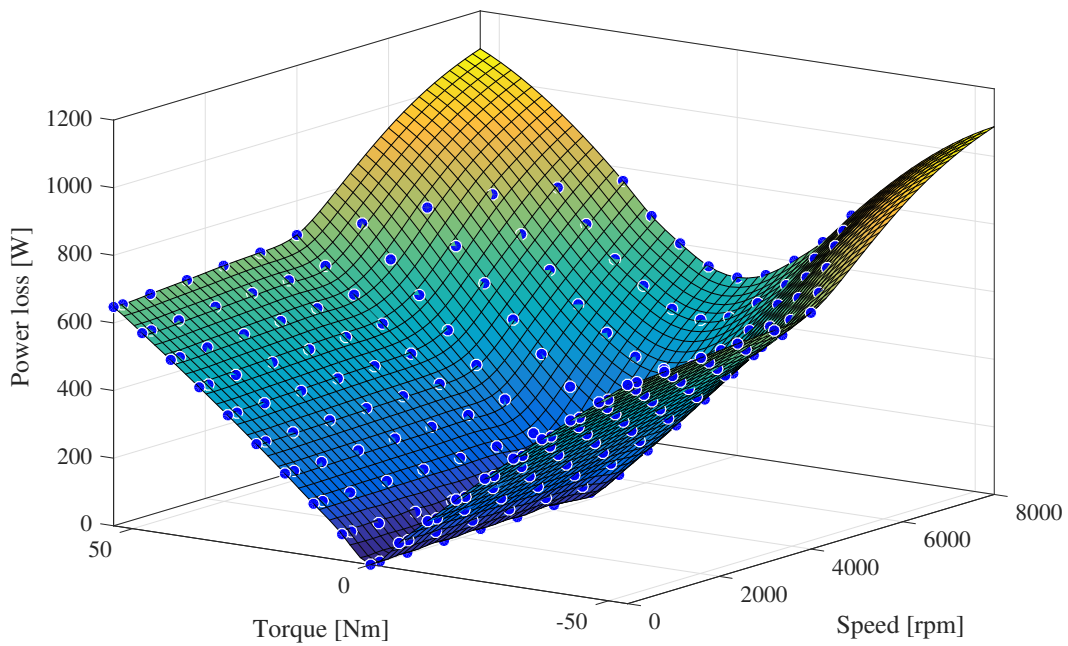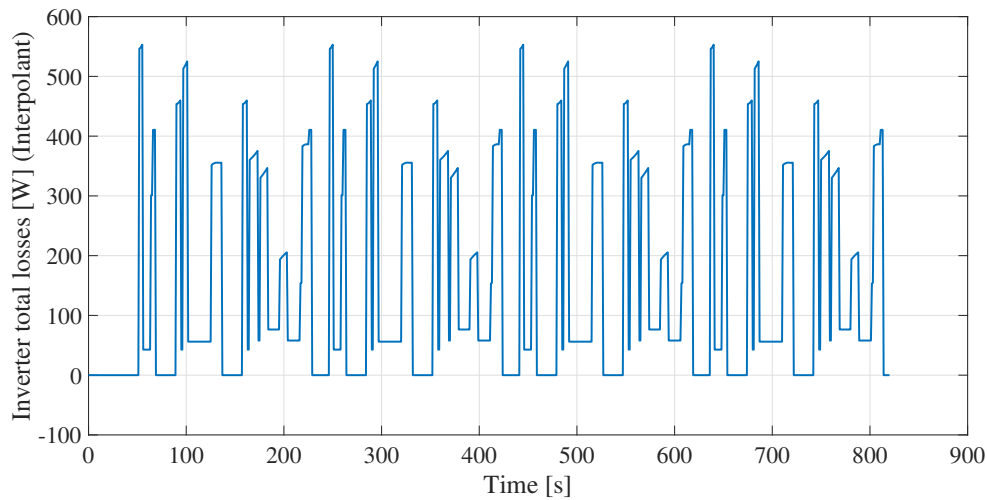

Figure 5.30: ECE total loss variation with time for SVM (NNET)

Apart from using NNET, interpolation method can be easily applied to do the prediction as well. The resulting plot is shown in Fig. 5.31.

Figure 5.31: Interpolation result for SVM

The inverter total loss versus time with a SVM model under ECE driving cycle using interpolant is plotted in Fig. 5.32. After integrating the curve, the total energy loss W is calculated to be $0.0340[kWh]$, which is very close to the result from NNET method. When performing the interpolation, the target function should pass through all given sample data points, whereas in the NNET curve fitting, the goal is to find the general trend only. Thus, the two methods could possibly lead to slight different result.

Figure 5.32: ECE total loss variation with time for SVM (Interpolation)

Similarly, the whole analysis above can be repeated for a DPWM method for comparison, taking DPWM3 for example. Again, the operating points of an ECE driving cycle are marked in the total loss map of DPWM3 method in Fig. 5.33.
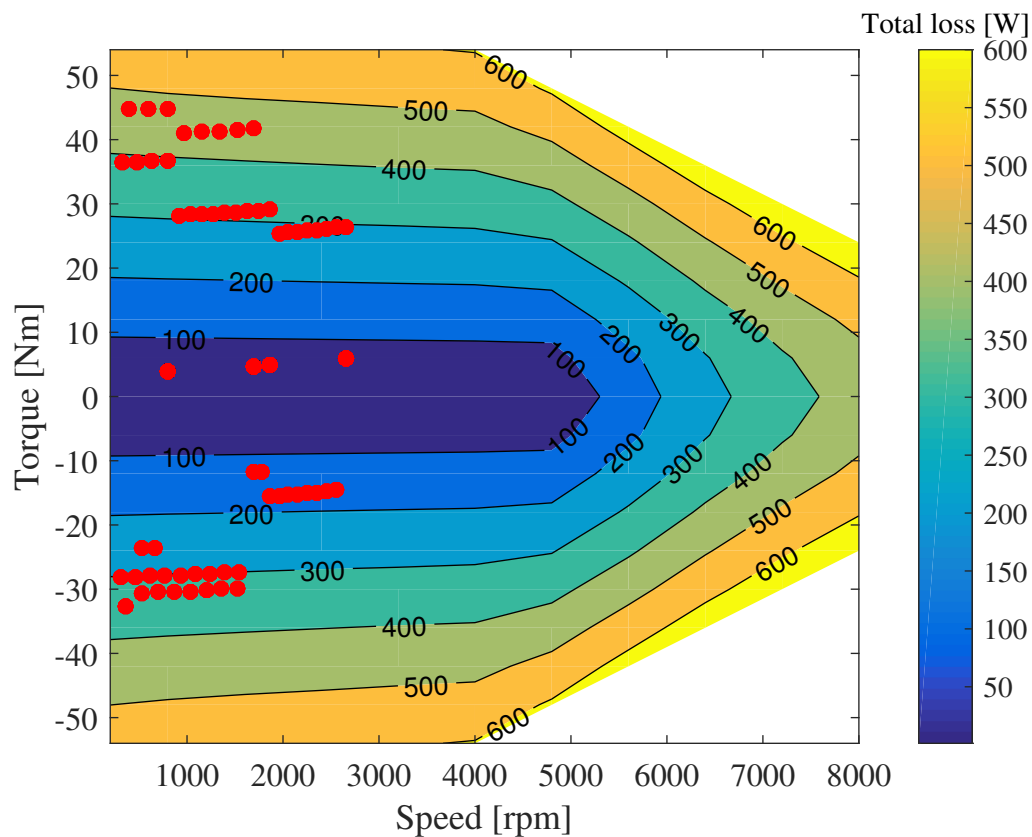
Figure 5.33: ECE operating points on DPWM3 total loss map

Again, the neural network curve fitting method is applied and the training results are omitted. The inverter total loss versus time with a DPWM3 model under ECE

driving cycle is plotted in Fig. 5.34. After integrating the curve, the total energy loss W is calculated to be 0.0290 $[kWh]$.
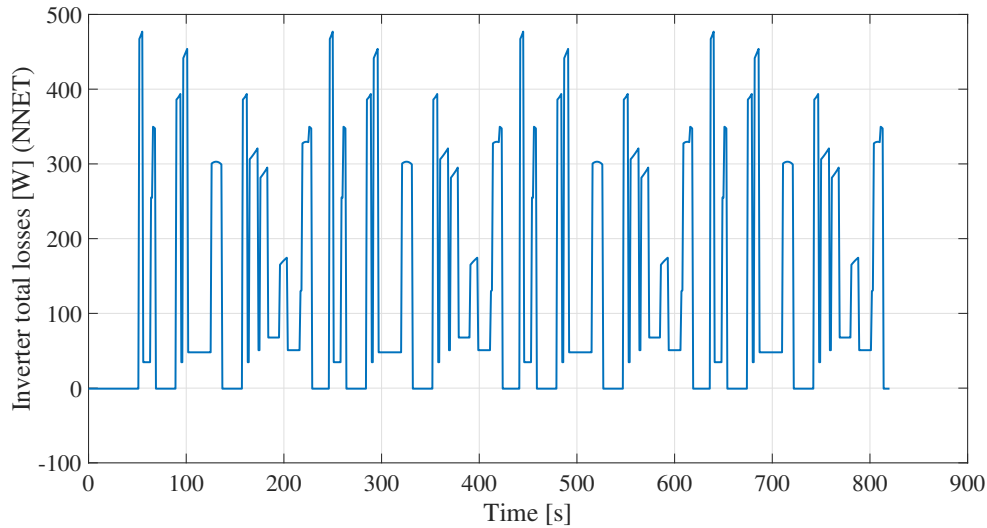
Figure 5.34: ECE total loss variation with time for DPWM3 (NNET)

Then interpolation method is used to do the data prediction for inverter total loss of DPWM3 method under ECE driving cycle. The result is shown in Fig. 5.35.

Figure 5.35: Interpolation result for DPWM3

The inverter total loss versus time with a DPWM3 model under ECE driving cycle using interpolant is plotted in Fig. 5.36. After integrating the curve, the total energy loss W is calculated to be 0.0289 $[kWh]$, which is again very close to the result from NNET method.

Figure 5.36: ECE total loss variation with time for DPWM3 (Interpolation)

5.3.2 EUDC

Now, the EUDC driving cycle is going to replace ECE to further evaluate the inverter loss performance of SVM and DPWM3. First, for SVM, the operating points of an EUDC driving cycle are marked in the total loss map of SVM method in Fig. 5.37.

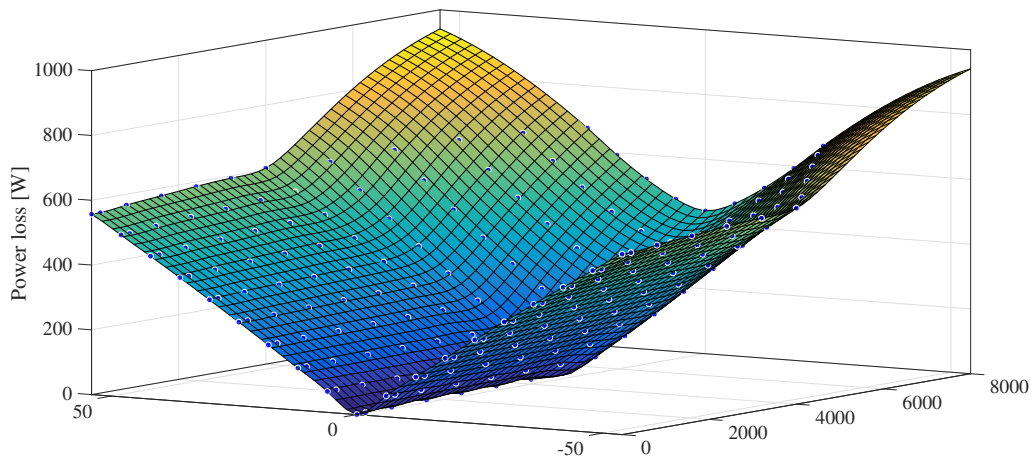**Figure 5.37:** EUDC operating points on SVM total loss map

Using NNET curve fitting method first, the inverter total loss versus time plot is shown in Fig. 5.38. The total energy loss W is 0.0227 $[kWh]$ after integration.
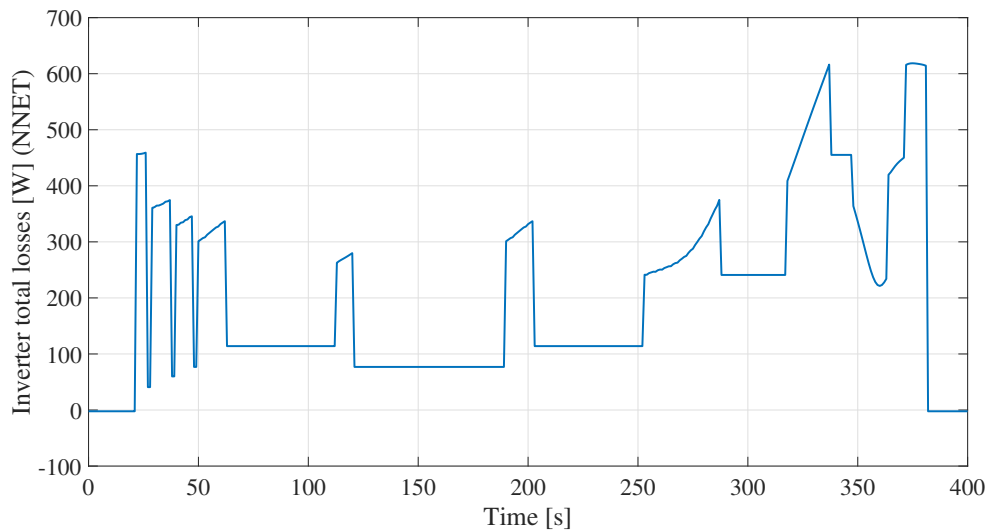
Figure 5.38: EUDC total loss variation with time for SVM (NNET)

Then the interpolation method is implemented for SVM under EUDC driving cycle. The inverter total loss variation with time is plotted in Fig. 5.39 for SVM method

under EUDC driving cycle. The total energy loss W is calculated to be 0.0227 $[kWh]$.

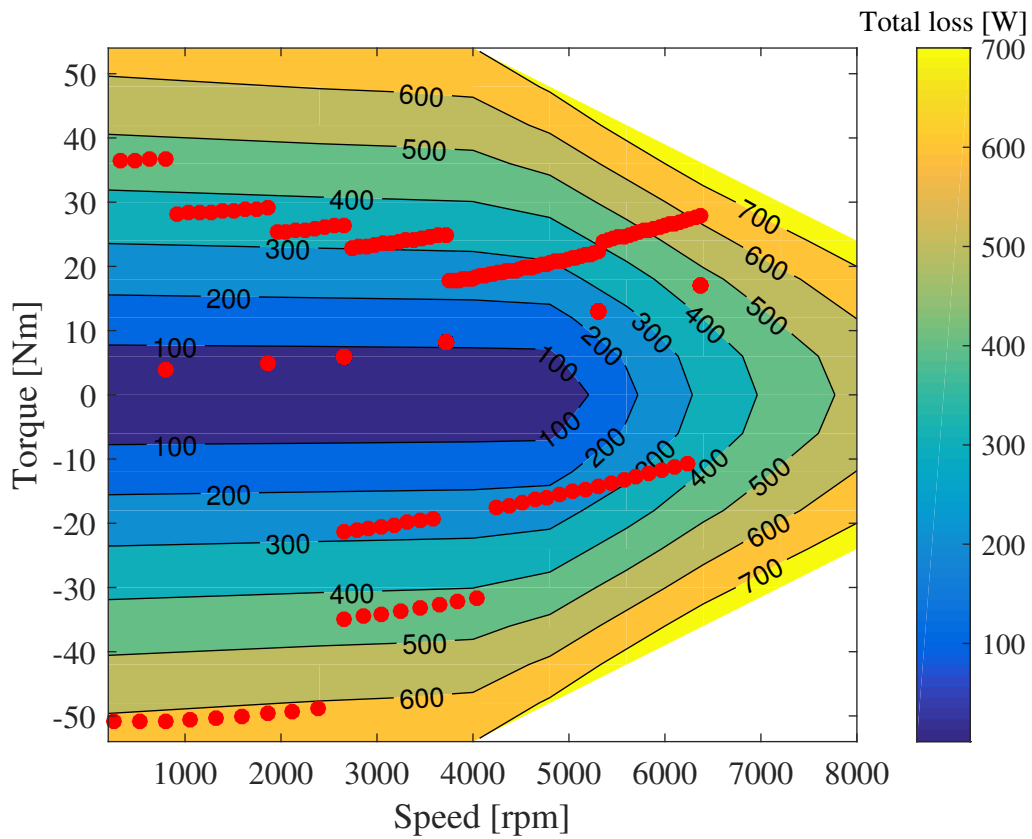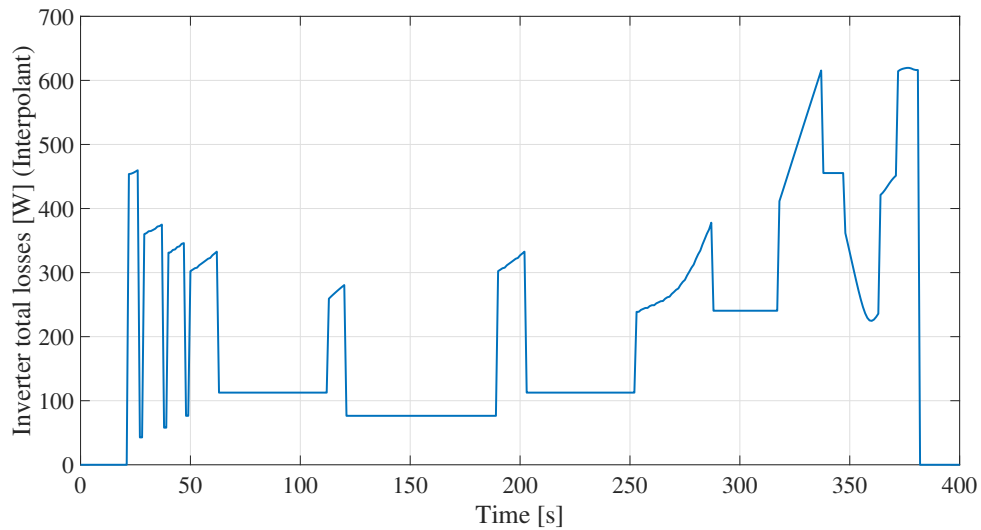**Figure 5.39:** EUDC total loss variation with time for SVM (Interpolation)

Similarly, the operating points of an EUDC driving cycle are marked red in the loss map of DPWM3 method, as is shown in Fig. 5.40.

Figure 5.40: EUDC operating points on DPWM3 total loss map

After the NNET curve fitting is applied, the total loss from DPWM3 method under EUDC driving cycle varies with time as is shown in Fig. 5.41. After integrating, the total energy loss W is measured to be $0.0195 \, [kWh]$.

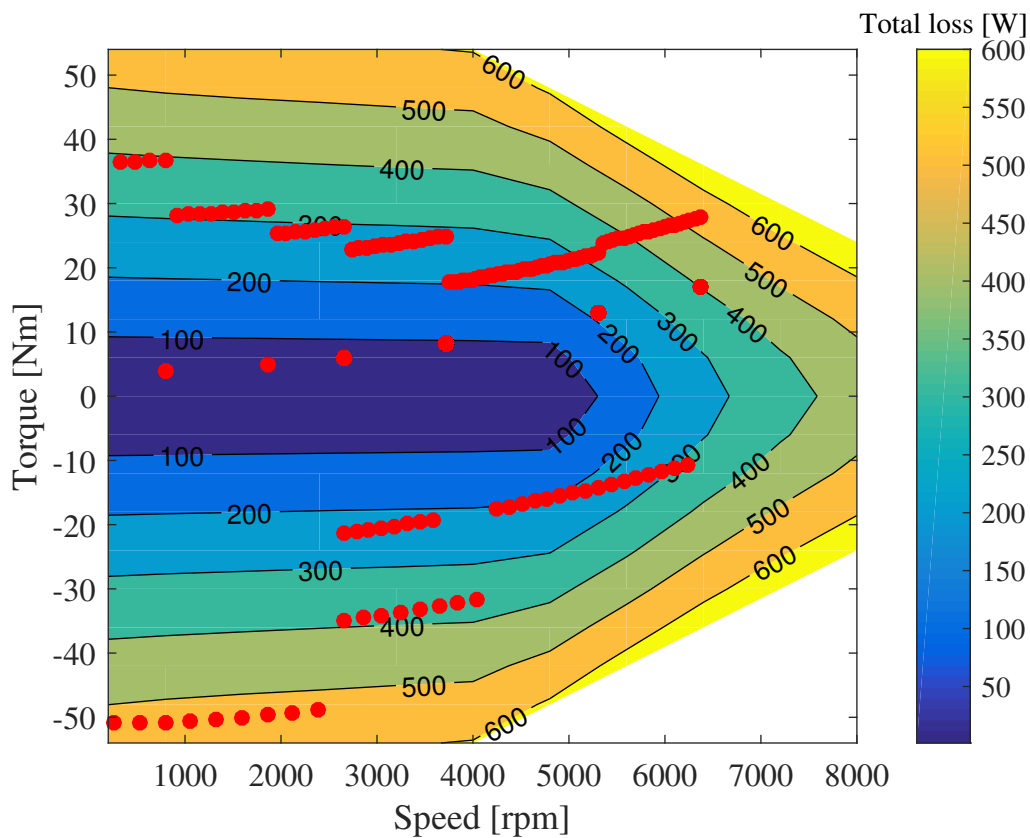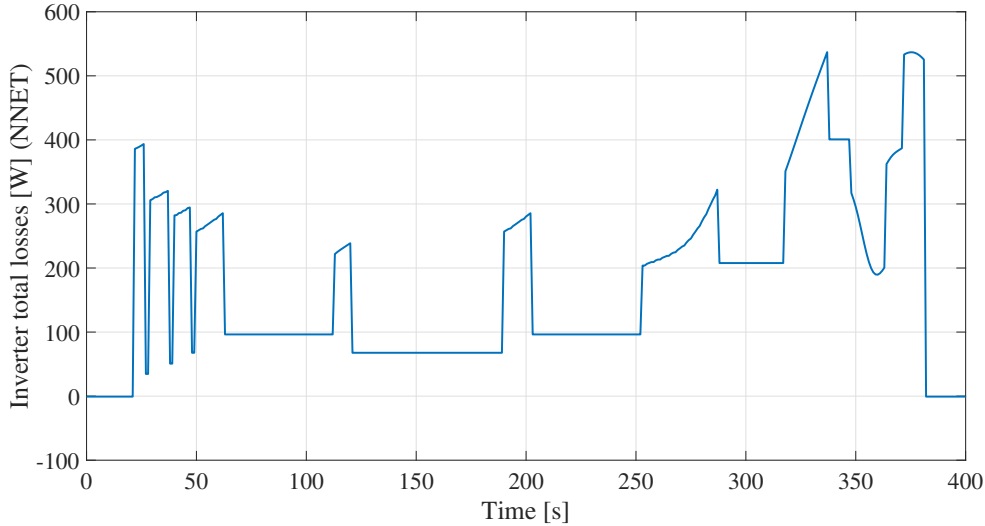**Figure 5.41:** EUDC total loss variation with time for DPWM3 (NNET)

Then the interpolation method is implemented for DPWM3 under EUDC driving cycle. The inverter total loss variation with time is plotted in Fig. 5.42 for DPWM3 method under EUDC driving cycle. The total energy loss W is calculated to be $0.0195 \, [kWh]$.
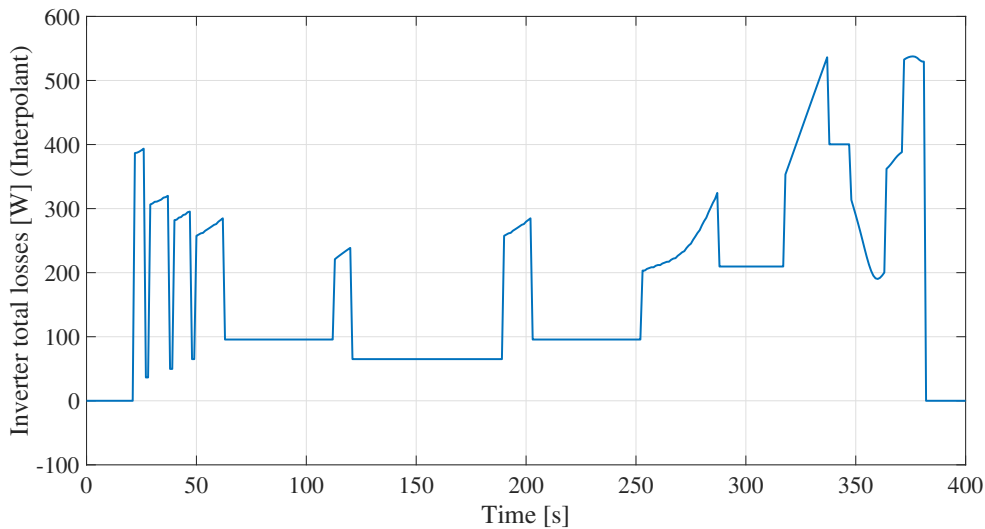
Figure 5.42: EUDC total loss variation with time for DPWM3 (Interpolation)

To conclude, all the results above are gathered in the table below. DPWM is proved to have lower inverter losses than CPWM in simulations close to a practical scenario. For ECE, DPWM3 has a 14.45 % total loss reduction compared to SVM; for EUDC, the reduction is 14.10 %.

Table 5.2: POWER LOSS COMPARISON BASED ON DRIVING CYCLES

| Driving Cycles	Modulation Strategies	Prediction Methods	Inverter Total Energy Losses [kWh]
ECE	SVM	NNET	0.0338
		Interpolation	0.0340
	DPWM3	NNET	0.0290
		Interpolation	0.0289
EUDC	SVM	NNET	0.0227
		Interpolation	0.0227
	DPWM3	NNET	0.0195
		Interpolation	0.0195

5.4 Comparison based on switching frequency

As is known from the previous chapter, discontinuous PWM shows an advantage over continuous PWM with lower switching losses. When the switching frequency varies, this conclusion can be further proved. SVM is used to represent continuous PWM next. The system is set to operate under 2400rpm and 42Nm for instance. At different operating points, the switching losses of different DPWM methods will vary drastically according to the analysis in Chapter 5.2.2. Figure 5.43, Fig. 5.44 and Fig. 5.45 show how inverter switching losses, conduction losses and total losses vary with switching frequency respectively.
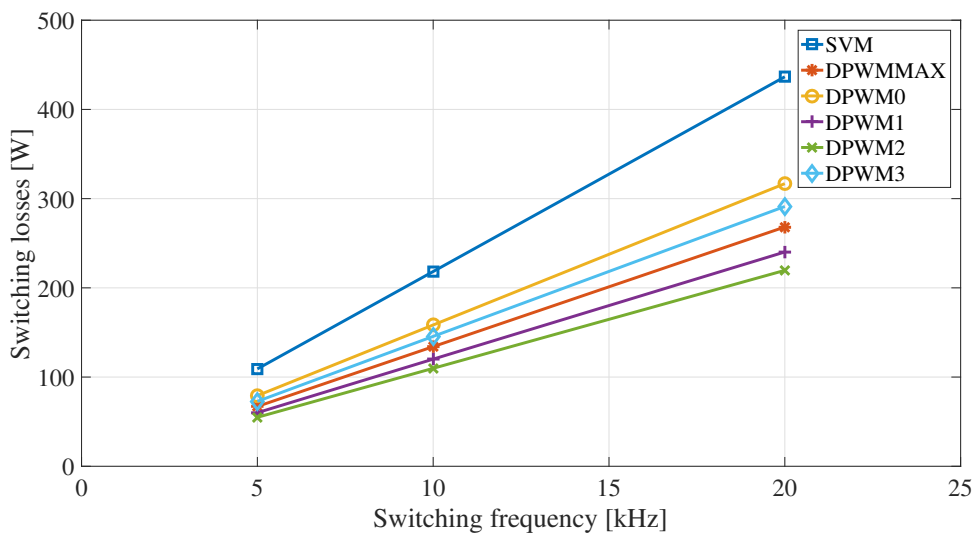
Figure 5.43: Switching losses comparison of SVM and DPWM methods based on different switching frequencies
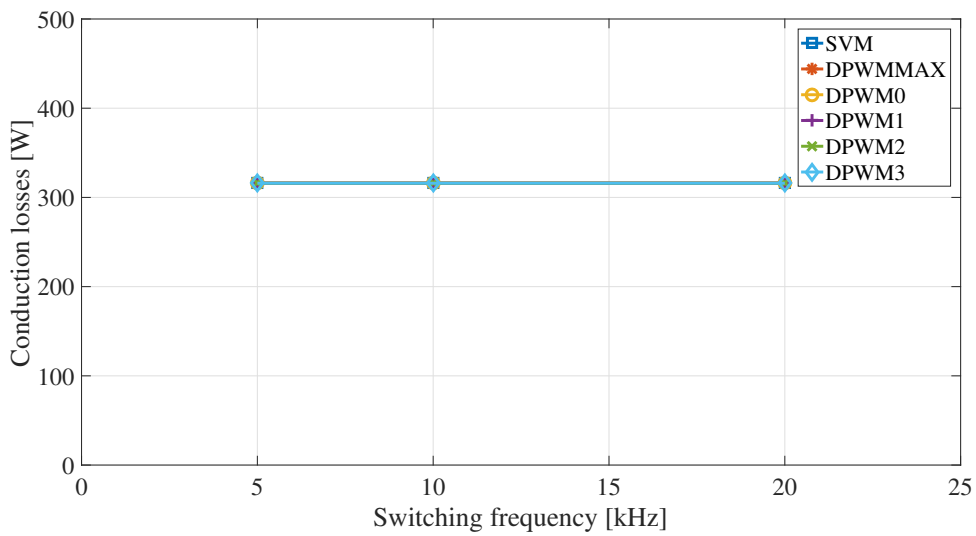
Figure 5.44: Conduction losses comparison of SVM and DPWM methods based on different switching frequencies
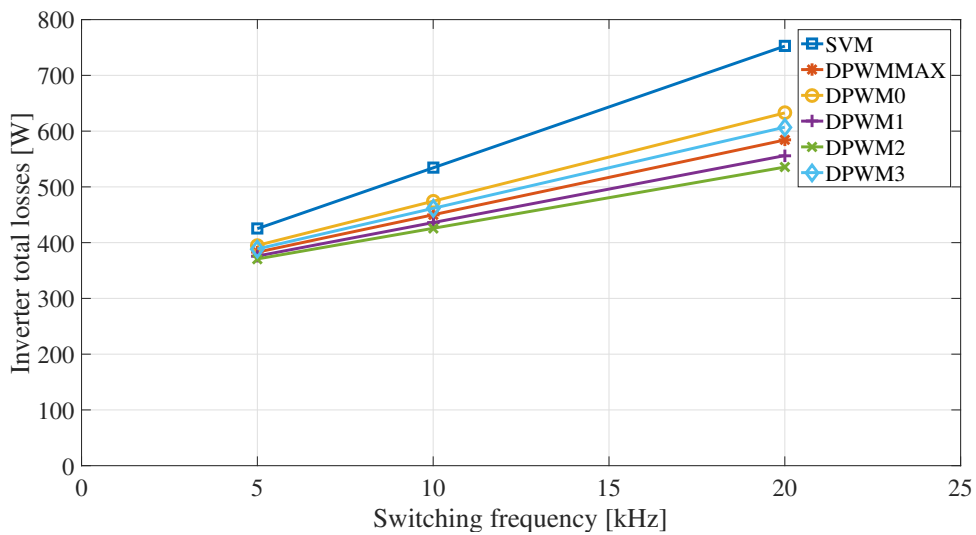
Figure 5.45: Inverter total losses comparison of SVM and DPWM methods based on different switching frequencies

At the same operating point, with a higher switching frequency, the current THD can be reduced, as is shown in Fig. 5.46.
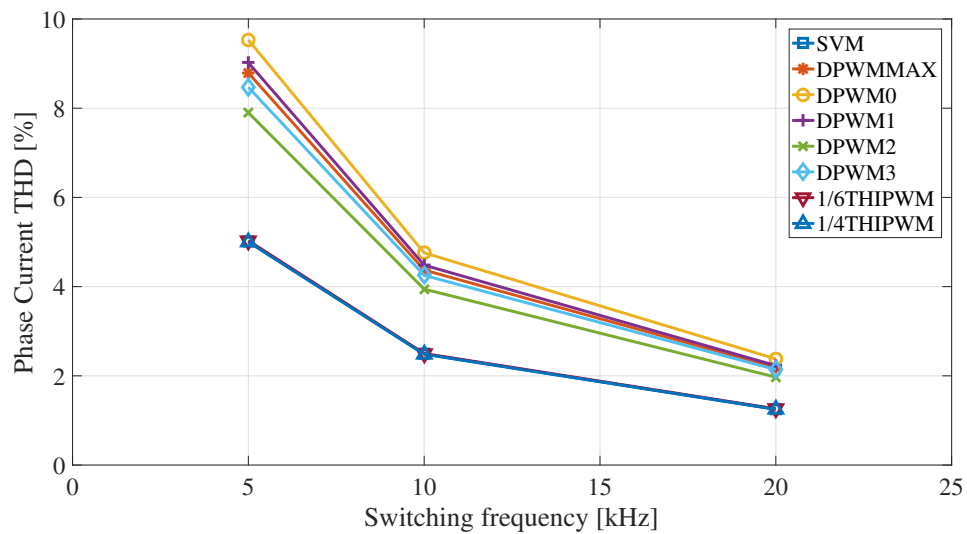
Figure 5.46: Current THD comparison based on different switching frequencies

From the figures above, it is clear that conduction losses do not differ much with different switching frequencies as the simulation model is simply a mathematical one. However, switching losses are proportional to switching frequencies and the advantage of DPWM is even larger with a higher switching frequency.

However, it is always a trade-off for discontinuous PWM. In order to compensate the high harmonic distortions caused by discontinuous modulation and take advantage of the low switching losses, higher switching frequency can be applied to DPWM methods to lower the harmonics at the expense of weakening the advantage of low switching losses.

6
Conclusion

In this thesis, modulation techniques including third-harmonic injection PWM, space-vector PWM and multiple discontinuous PWM methods are studied and implemented into the existing PMSM field-oriented control system. The characteristic waveforms are observed and MTPA is explained in details. Key parameters including current total harmonic distortion, inverter conduction losses, switching losses and efficiency are measured and calculated. These results are post-processed and plotted in a speed-torque PMSM operating map and the derived maps are compared and analyzed in details. Furthermore, driving cycle tests are conducted to evaluate the previous results more practically. Switching frequency tests are done to further investigate into the losses' sensitivity to switching frequency.

From the current THD simulation results, it can be concluded that in general continuous PWM methods have lower harmonics than discontinuous ones. However, DPWM2 is found to behave even better than 1/4 THIPWM, which has the lowest THD among the continuous PWM methods investigated, in the high-speed region of the map. From the inverter losses comparison, the conclusion is that the conduction losses are the same for all modulation methods in this model, but for switching losses, the results clearly show that DPWM has an advantage over CPWM. When DPWM methods are compared with each other, the phase angle plays a significant role in it. Therefore, in different regions of the map, different DPWM methods could be the most favorable one. A lower switching loss means higher inverter efficiency.

Neural network curve fitting and interpolation are both applied to find out the real-time energy losses in an ECE or EUDC driving cycle. Results from curve fitting and interpolation converge and further prove that DPWM consumes less power than CPWM in a driving cycle test, cutting the losses by approximately 14 %. A switching frequency variation from 5 kHz to 20 kHz shows that the switching loss difference between DPWM and CPWM is larger, proportional to switching frequency. In order to compensate the high harmonic distortions caused by discontinuous modulation and take advantage of the low switching losses, higher switching frequency can be applied to DPWM methods to lower the harmonics at the expense of weakening the advantage of low switching losses.

References

[1] Y.-j. Yu, F. Chai, and S.-K. Cheng, "Analysis of modulation pattern and losses in inverter for pmsm drives," in *Vehicle Power and Propulsion Conference, 2008. VPPC'08. IEEE.* IEEE, 2008, pp. 1–4.

[2] Y. Wu, M. A. Shafi, A. M. Knight, and R. A. McMahon, "Comparison of the effects of continuous and discontinuous pwm schemes on power losses of voltage-sourced inverters for induction motor drives," *IEEE Transactions on Power Electronics*, vol. 26, no. 1, pp. 182–191, 2011.

[3] M. Bierhoff, H. Brandenburg, and F. W. Fuchs, "An analysis on switching loss optimized pwm strategies for three phase pwm voltage source converters," in *Industrial Electronics Society, 2007. IECON 2007. 33rd Annual Conference of the IEEE.* IEEE, 2007, pp. 1512–1517.

[4] J. Holtz, W. Lotzkat, and A. M. Khambadkone, "On continuous control of pwm inverters in the overmodulation range including the six-step mode," *IEEE Transactions on Power Electronics*, vol. 8, no. 4, pp. 546–553, 1993.

[5] A. M. Hava, R. J. Kerkman, and T. A. Lipo, "Carrier-based pwm-vsi overmodulation strategies: analysis, comparison, and design," *IEEE Transactions on Power Electronics*, vol. 13, no. 4, pp. 674–689, 1998.

[6] A. K. Gupta and A. M. Khambadkone, "A general space vector pwm algorithm for multilevel inverters, including operation in overmodulation range," *IEEE transactions on Power Electronics*, vol. 22, no. 2, pp. 517–526, 2007.

[7] ——, "A simple space vector pwm scheme to operate a three-level npc inverter at high modulation index including overmodulation region, with neutral point balancing," *IEEE Transactions on Industry Applications*, vol. 43, no. 3, pp. 751–760, 2007.

[8] D. G. Holmes and T. A. Lipo, *Pulse width modulation for power converters: principles and practice.* John Wiley & Sons, 2003, vol. 18.

[9] B. K. Suda and J. David, "'a novel third harmonic injection method for closed loop control of pmsm motors," *The Magazine of Electric Motor and Drive Technology*, pp. 1–4, 2015.

[10] P. Dushan, "Igbt power losses calculation using the data-sheet parameters," *Infineon, Appl. Note, V1. 1*, 2009.

[11] *IGBT module datasheet*, SEMIKRON, 08 2016, rev. 2.0.

[12] M. H. Bierhoff and F. W. Fuchs, "Semiconductor losses in voltage source and current source igbt converters based on analytical derivation," in *Power Electronics Specialists Conference, 2004. PESC 04. 2004 IEEE 35th Annual*, vol. 4. IEEE, 2004, pp. 2836–2842.

[13] A. M. Hava, R. J. Kerkman, and T. A. Lipo, "Simple analytical and graphical methods for carrier-based pwm-vsi drives," *IEEE transactions on power electronics*, vol. 14, no. 1, pp. 49–61, 1999.

[14] ——, "A high-performance generalized discontinuous pwm algorithm," *IEEE Transactions on Industry applications*, vol. 34, no. 5, pp. 1059–1071, 1998.

[15] Wikipedia, "New European Driving Cycle — Wikipedia, the free encyclopedia," http://en.wikipedia.org/w/index.php?title=New%20European%20Driving%20Cycle&oldid=845017943, 2018, [Online; accessed 07-August-2018].

[16] L. Guzzella and C. Onder, *Introduction to modeling and control of internal combustion engine systems.* Springer Science & Business Media, 2009.

[17] D.-W. Chung, J.-S. Kim, and S.-K. Sul, "Unified voltage modulation technique for real time three-phase power conversion," in *Industry Applications Conference, 1996. Thirty-First IAS Annual Meeting, IAS'96., Conference Record of the 1996 IEEE*, vol. 2. IEEE, 1996, pp. 921–926.

[18] Wikipedia, "Artificial neural network — Wikipedia, the free encyclopedia," http://en.wikipedia.org/w/index.php?title=Artificial%20neural%20network&oldid=860543192, 2018, [Online; accessed 22-September-2018].